# Wireless-Coupled Oscillator Systems With an Injection-Locking Signal

Mabel Pontón, *Member, IEEE*, Amparo Herrera, and Almudena Suárez, *Fellow, IEEE*

***Abstract*— A detailed analysis of wireless-coupled oscillator systems under the effect of an injection-locking signal is presented. The injection source of high spectral purity is introduced at a single node and enables a reduction of the phase-noise spectral density. Under this injection source, the behavior of the coupled system is qualitatively different from the one obtained in free-running conditions. Two cases are considered: bilateral synchronization, in which an independent source is connected to a particular system oscillator, coupled to the other oscillator elements, and unilateral synchronization, in which one of these elements is replaced by an independent source that cannot be influenced by the rest. The two cases are illustrated through the analysis of a wireless-coupled system with a star topology, such that the injection signal is introduced at the central node. The investigation involves an insightful analytical calculation of the coexisting steady-state solutions, as well as a determination of their stability and bifurcation properties and phase noise. The injection signal stabilizes the system in a large and continuous distance interval, enabling a more robust operation than in autonomous (non-injected) conditions. A coupled system operating at 2.45 GHz has been manufactured and experimentally characterized, obtaining very good agreement between simulations and measurements.**

***Index Terms* — Injection locking, phase noise, stability, wireless-coupled oscillators.**

## I. Introduction

SYNCHRONIZATION is an essential requirement in sensor networks, multiple-input multiple output (MIMO) antenna systems, measurement systems, and other [1]-[10]. In sensor networks, this synchronization enables cooperative transmissions, data-fusion of time-sensitive measurements or moving object tracking. When using packets carrying time stamps [1] random delays may occur in the construction and processing of the packet. An alternative methodology [1]-[12] would rely on the wireless coupling of the oscillators in the network nodes. There are two different coupling methods: through pulses [6], [8]-[9] and through a continuous phase locking of the oscillator signals [1], [10]-[12]. The pulse coupling is achieved transmitting a pulse and detecting its arrival time, which involves a fast time scale, associated to the short-duration pulse, and a slow one, associated to the evolution of the oscillator phase. The system is analyzed in terms of maps, using discrete-time models [3]. In phase coupling [1], [10]-[12] the oscillator nodes transmit and receive continuously, so continuous models are used, enabling a more detailed comprehension of the system behavior. In the limit of weak coupling, the two methodologies exhibit substantial analogies, as demonstrated in [5], [13].

One should emphasize that the behavior of the wireless-coupled system [14]-[15] is qualitatively very different from the one obtained in coupled-oscillator systems for beam steering applications [16]-[24]. In the beam-steering arrays, the oscillators are coupled through circuits, usually composed by a transmission line bounded by resistors [16]-[19]. In the wireless case [14]-[15], the coupling coefficients depend on the antenna gain and propagation effects. When modifying the distance between the oscillator elements, they undergo significant amplitude and phase variations, with a strong impact on the system solution pattern and stability properties.

Most previous works on wireless coupled oscillators [1]-[13], rely on simplified mathematical models [2]-[3], with the oscillator circuits represented in terms of phase variables, and the coupling terms consisting of constant scalar coefficients and time delays. In the recent works [14]-[15] a detailed formulation is presented for wireless coupled-oscillator systems in free-running (or autonomous) conditions, which enables the investigation of all the basic configurations [15] used in sensor networks [3], [7]-[8]. The formulation in [14]-[15] is based on a realistic description of the coupled system, such that the oscillator elements are represented with accurate models, extracted from harmonic-balance (HB) and the coupling effects are thoroughly described in terms of the operation frequency, distance and antenna gain. As stated, the analysis of [14]-[15] is limited to coupled systems in which none of the oscillator components is subject to an injection-locking source, as widely considered in previous research on distributed synchronization of sensor networks. However, the works [25]-[27] address coupled systems with a reference timing signal, introduced into one or more oscillator elements, which can be easily done through injection locking or phase locking. A reference signal with a high spectral purity will reduce the phase noise in all the system oscillators, due to the wireless coupling. Despite the need for a low phase noise in most practical applications, there is little information on the performance of the wireless-coupled system under an injection signal. The investigation of this

Manuscript received June 8, 2018. This work was supported by the Spanish Ministry of Economy and Competitiveness and the European Regional Development Fund (ERDF/FEDER) under research projects TEC2014-60283-C3-1-R and TEC2017-88242-C3-1-R.

M. Pontón, A. Herrera and A. Suárez are with the Departamento de Ingeniería de Comunicaciones, Universidad de Cantabria, Santander, 39005, Spain (e-mail: mabel.ponton@unican.es; amparo.herrera@unican.es; almudena.suarez@unican.es).

performance is the focus of this work, which will address the system steady-state solutions and solution curves, as well as their stability properties and phase noise.

The investigation will be based on a formulation of the coupled system using realistic models for the oscillator elements extracted from HB. The system will be analytically resolved, deriving closed-form expressions. This will enable a valuable insight into the impact of the particular oscillator design and propagation effects on the solution pattern versus the distance between the oscillator elements and other parameters. Two cases are considered. The first one, here denoted as "bilateral injection", is a coupled system in which one of the oscillator elements is injection-locked by an independent source. The second case, denoted as "unilateral injection", is a coupled system in which one of the oscillator elements is replaced by an independent source that cannot be influenced by the rest.

The bilateral injection is of interest in networks of arbitrary topology, since it minimizes the degradation in the system symmetry. As will be shown, when increasing the amplitude of the injection source from zero value, distinct synchronization intervals arise about the particular distance values at which the free-running frequency of the coupled system agrees with that of the injection source. As the source amplitude increases, a value is reached, such that stable operation is obtained for all the distance values up to a certain maximum. This is a fundamental difference with respect to the behavior in free-running conditions [15], i.e., in the absence of the synchronizing source [14]-[15], in which stable and unstable intervals alternate. The stable operation in a large and continuous distance range enhances the system robustness and facilitates its practical application. In the unilateral case, the central oscillator is replaced with an independent source. In a manner similar to the bilateral case, the synchronized behavior is maintained only up to a maximum distance value, though the variation of the oscillation amplitude versus the distance is qualitatively different in the two cases.

The paper is organized as follows. Section II presents the investigation of the bilateral case, including stability and phase noise. Section III describes the analysis of the unilateral case, also including stability and phase-noise properties.

## II. Bilateral Injection

The investigation will be illustrated through its application to a system with a star topology. Nevertheless, it can easily be extended to an arbitrary symmetric topology, as described in subsection *B*. In the arbitrary case, an analogous analysis should be applied to each oscillation mode (resulting from the system symmetry [14]-[15]), which would complicate the study without adding any additional insight.

Let a system of $M$ wireless coupled oscillators with a star topology be considered [Fig. 1(a)]. The central node is coupled to the surrounding $M$–1 oscillators (at a distance $d$ from the central one) and each of these oscillators is coupled to the central one only. This central oscillator will also be injection locked by an independent source at the frequency $\omega_s$, with a small current amplitude $I_g$ [Fig. 1(b)].

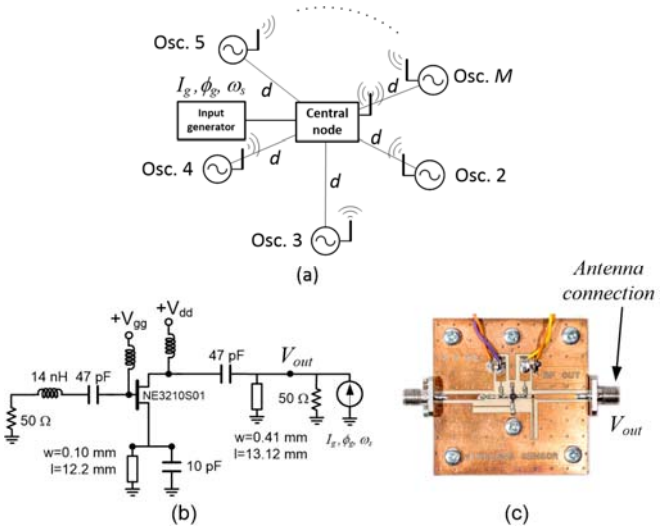


Fig. 1. Star topology. (a) Coupled network. (b) Schematic of the individual oscillator. For better insight, the injection signal is introduced at the output port, which enables a simpler formulation. The input resistor corresponds to the input impedance of a spectrum analyzer (c) Prototype built on Rogers 4003C.

### A. Steady-state solution

Assuming a synchronized solution at the injection-source frequency $\omega_s$, the network in Fig. 1(a) is governed by the following system of steady-state equations:

$$\begin{aligned} Y(V_1,\omega_s)V_1 &= (M-1)\,C_L\,V_2 e^{j\phi_2} + I_g e^{j\phi_g} \\ Y(V_2,\omega_s)V_2 e^{j\phi_2} &= C_L\,V_1 \end{aligned} \tag{1}$$

where $V_1$ is the oscillation amplitude at the central element, the phase origin is taken at the central oscillator and $V_2$ and $\phi_2$ are the amplitude and phase at the rest of oscillator elements, assumed equal. The whole system operates at the frequency of the injection-locking source $\omega_s$. The central oscillator exhibits a phase shift $-\phi_g$ with respect to this injection source. The function $Y$ is the current-to-voltage ratio of each oscillator, seen from the coupling node, and $C_L$ is the complex coupling coefficient, depending on the antenna gain and propagation effects, with admittance dimension. As derived in [15], [28], the coefficient $C_L$ is given by:

$$C_L(d,\omega_s) = \frac{c}{\omega_s R_r d}\sqrt{G_{tot}}\,e^{-j\frac{d}{c}\omega_s} = Ae^{-j\alpha} \tag{2}$$

where $G_{tot}$ is the product of the two antenna gains, $R_r$ the radiation resistance, $c$ the speed of light and $d$ the distance to the central oscillator. Note that the wrapped phase is periodic with the period $d = \lambda$, which will have an impact on the shape of solution curves versus $d$, exhibiting a tendency to periodicity.

The crucial difference between (1) and the analyses in [14]-[15] is the presence of the injection-locking source at the central-node oscillator, which, as will be shown, will enable a reduction of the system phase-noise spectral density and a continuous distance interval with stable behavior. The central oscillator must respond to two distinct types of injection signals: the low-amplitude signal from the independent source and the coupling signals from the rest of oscillator elements. Due to the low injection amplitude $I_g$ and the attenuation resulting from the propagation loss, the oscillator elements

(assumed equal) will only undergo small deviations with respect to their original free-running solution, when isolated form the rest. The free-running amplitude and frequency are $V_o$ and $\omega_o$, respectively. Thus, it will be possible to perform a first-order Taylor series expansion of the admittance function $Y(V,\omega_s)$ in (1) about the free-running point ($V_o$, $\omega_o$) [20]-[22]. Splitting the resulting complex equations into real and imaginary parts, one obtains:

$$H_1 = Y_v^r\ \Delta V_1 + Y_\omega^r \Delta\omega_s - A'\cos(\phi_2') - \frac{I_g}{V_o}\cos(\phi_g) = 0 \qquad (3a)$$

$$H_2 = Y_v^i\ \Delta V_1 + Y_\omega^i \Delta\omega_s - A'\sin(\phi_2') - \frac{I_g}{V_o}\sin(\phi_g) = 0 \qquad (3b)$$

$$H_3 = Y_v^r\ \Delta V_2 + Y_\omega^r \Delta\omega_s - A\cos(\phi_2'') = 0 \qquad (3c)$$

$$H_4 = Y_v^i\ \Delta V_2 + Y_\omega^i \Delta\omega_s - A\sin(\phi_2'') = 0 \qquad (3d)$$

where the second-order terms have been neglected and the following variables have been defined: $A' = (M-1)A$, $\phi_2' = \phi_2 - \alpha$ and $\phi_2'' = -\phi_2 - \alpha$. The subscript indicates the variable with respect to which each derivative is calculated and the superscript indicates real or imaginary part. The increments are $\Delta V_1 = V_1 - V_o$, $\Delta V_2 = V_2 - V_o$, $\Delta\omega_s = \omega_s - \omega_o$. Note that system (3) is nonlinear in the two phases $\phi_2$ and $\phi_g$.

The derivatives $Y_v$, $Y_\omega$ only depend on the particular design of the original free-running oscillator. They are calculated by introducing an auxiliary generator (AG) in the HB simulator and applying finite differences [20], [29]. The AG is a voltage generator operating at the unknown oscillation frequency $\omega$, with the amplitude $V$. It is connected in series with an ideal bandpass filter at $\omega$ and introduced in parallel at a circuit node. The AG musts fulfill the steady-state oscillation condition, $Y(V_o, \omega_o) = 0$, where $Y$ is the ratio between the AG current and voltage. Once this condition is fulfilled, the node amplitude at the fundamental frequency $\omega_o$ will agree with $V_o$.

To extract the oscillator model, the AG will be introduced in parallel at the node where the oscillator circuit is connected to the antenna. Using ($V_o$, $\omega_o$) as quiescent point, the amplitude derivative $Y_v$ is obtained by setting the AG amplitude to $V_o+\Delta V$, while its frequency is kept at $\omega_o$. Then, a circuit-level HB simulation is carried out, considering the whole circuit, with all its parasitics, and harmonic terms. The derivative $Y_v$ is calculated as $Y_v = Y/\Delta V$, where $Y$ is the value of the admittance function after the application of $\Delta V$. The frequency derivative $Y_\omega$ is obtained by setting the AG frequency to $\omega_o+\Delta\omega$, while its amplitude is kept at $V_o$. The derivative $Y_\omega$ is calculated as $Y_\omega = Y/\Delta\omega$, where $Y$ is the value of the admittance function after the application of $\Delta\omega$.

For a given frequency of the synchronizing source, $\Delta\omega_s$ is known in (3). In these conditions, system (3) can be solved analytically. Squaring equations (3c) and (3d) and adding the results, one obtains:

$$|Y_v|^2 \Delta V_2^2 + 2P_{v\omega}\Delta\omega_s\Delta V_2 + |Y_\omega|^2 \Delta\omega_s^2 = A^2 \qquad (4)$$

where:

$$P_{v\omega} = Y_v^r Y_\omega^r + Y_v^i Y_\omega^i = |Y_v||Y_\omega|\cos\alpha_{v\omega} \qquad (5)$$

The angle $\alpha_{v\omega} = \alpha_\omega - \alpha_v$ is the difference between the phase $\alpha_\omega$ of $Y_\omega$ and the phase $\alpha_v$ of $Y_v$. Then it is possible to solve for $\Delta V_2$ in terms of $\Delta\omega_s$, which provides:

$$\Delta V_2 = \frac{-|Y_\omega|\cos\alpha_{v\omega}\Delta\omega_s \pm \sqrt{-|Y_\omega|^2\Delta\omega_s^2\sin^2\alpha_{v\omega} + A^2}}{|Y_v|} \qquad (6)$$

To obtain real solutions for $\Delta V_2$ the radicand must be positive. This radicand increases with the magnitude of the coupling admittance $A$ and decreases with the shift $|\Delta\omega_s|$ with respect to $\omega_o$ and the oscillator quality factor (leading to a higher $|Y_\omega|$). On the other hand, $\Delta V_2$ can be negative since it is the amplitude deviation with respect to the free-running value. Using (3c) and (3d), a distinct phase value $\phi_2'' = -\phi_2 - \alpha$ is obtained for each $\Delta V_2$. Thus, there are two solutions in terms of the pair of variables $\Delta V_2, \phi_2$. Replacing each solution into (3a) and (3b), one can get the remaining variables: $\Delta V_1, \phi_g$. We solve first for $\Delta V_1$ by squaring (a) and (b) and adding the results, which provides:

$$|Y_v|^2 \Delta V_1^2 + 2\left(P_{v\omega}\Delta\omega_s + A'P_{v\phi}\right)\Delta V_1 + 2A'P_{\omega\phi}\Delta\omega_s + |Y_\omega|^2\Delta\omega_s^2 + A'^2 - \left(\frac{I_g}{V_o}\right)^2 = 0 \qquad (7)$$

where the following terms have been introduced:

$$P_{v\phi} = -Y_v^r\cos(\phi_2') - Y_v^i\sin(\phi_2') = -|Y_v|\cos(\phi_2' - \alpha_v)$$
$$P_{\omega\phi} = -Y_\omega^r\cos(\phi_2') - Y_\omega^i\sin(\phi_2') = -|Y_\omega|\cos(\phi_2' - \alpha_\omega) \qquad (8)$$

To obtain a real value of $\Delta V_1$ in (7), the following radicand must be positive:

$$(I_g/V_o)^2 - A'^2\sin^2(\phi_2' - \alpha_{v\omega}) + 2A'|Y_\omega|\Delta\omega_s\left(\cos(\alpha_{v\omega}) - 1\right)\cos(\phi_2' - \alpha_{v\omega}) - |Y_\omega|^2\sin^2\alpha_{v\omega}\Delta\omega_s^2 > 0 \qquad (9)$$

A comparison of the quantity (9) with the radicand of (6) evidences the opposed effects of the coupling signals ($A'$) and the independent synchronizing signal ($I_g$). Under a sufficiently small $|\Delta\omega_s|$, a high positive value of $(I_g/V_o)^2 - A'^2$ ensures the existence of steady-state solutions at the source frequency $\omega_s$. However, a relatively high value of $A' = (M-1)A$ is required to obtain a valid solution from (6), depending on $A$. Due to the negative term $-|Y_\omega|^2\Delta\omega_s^2\sin^2\alpha_{v\omega}$ in (6) and (9), synchronized solutions can only be achieved in a certain interval of $\Delta\omega_s$. Note that the particular case $\sin\alpha_{v\omega} = 0$ would correspond to a turning-point bifurcation of the individual free-running oscillator [30], prior to its introduction into the coupled system.

From the inspection of (6) and (7), there will be two solutions

in terms of $\Delta V_1$ for each solution in terms of $\Delta V_2$ and $\phi_2$. The phase $\phi_g$ corresponding to each $\Delta V_1$ is directly obtained from (3a) and (3b). Therefore, for a given distance *d*, there will be four solutions in the central oscillator and two solutions in the surrounding oscillators. This agrees with the fact that only the central oscillator is connected to the independent synchronizing source. As will be shown, the shape of the solution curves versus the distance *d* can be complex since there is a double dependence on this distance, in the scalar *A* (inversely proportional to *d*), and in the propagation phase shift *α*.

In order to get some insight into the curve shape, one can initially assume a small amplitude $I_g$ of the input generator. In these conditions, there will be periodic solutions only in small *d* intervals, located about the particular distance values $d_{op}$, where $p = 1$ to $P$, at which the coupled system exhibits a free-running oscillation (with $I_g = 0$) at the particular frequency deviation $\Delta\omega_s = \omega_s - \omega_o$. To obtain these distance values, the synchronizing source is eliminated from (3), which provides the following free-running system:

$$Y_v^r \Delta V_1 + Y_\omega^r \Delta\omega_s = A'(\Delta\omega_s)\cos\left[\phi_2'(\Delta\omega_s)\right] \quad (10a)$$

$$Y_v^i \Delta V_1 + Y_\omega^i \Delta\omega_s = A'(\Delta\omega_s)\sin\left[\phi_2'(\Delta\omega_s)\right] \quad (10b)$$

$$Y_v^r \Delta V_2 + Y_\omega^r \Delta\omega_s = A(\Delta\omega_s)\cos\left[\phi_2''(\Delta\omega_s)\right] \quad (10c)$$

$$Y_v^i \Delta V_2 + Y_\omega^i \Delta\omega_s = A(\Delta\omega_s)\sin\left[\phi_2''(\Delta\omega_s)\right] \quad (10d)$$

where the dependence of both $A(\Delta\omega_s)$ and $\phi_2' = \phi_2 - \alpha(\Delta\omega_s)$ on $\Delta\omega_s = \omega_s - \omega_o$ is emphasized. The coupled system (10) behaves in an autonomous manner, so the synchronized frequency $\omega_s$ (and, thus, the deviation $\Delta\omega_s$) is an unknown of the problem. System (10) can only be numerically solved, which is done in terms of $\Delta V_1, \Delta V_2, \Delta\phi_2, \Delta\omega_s$ for each *d* value. From this analysis, one can gather all the distance values $d_{op}$, where $p = 1$ to $P$, such that $\Delta\omega_s$ agrees with the difference between the particular injection frequency $\omega_s$ and $\omega_o$.

In the presence of the synchronizing source, under small amplitude $I_g$, it will be possible to perform a Taylor-series expansion of (3) about each free-running solution, given by $d_{op}$ and $\phi_{2p}$. The linearized system is:

$$Y_v^r \delta V_1 - \frac{\partial(A'\cos\phi_2')}{\partial d}\delta d - \frac{\partial(A'\cos\phi_2')}{\partial\phi_2}\delta\phi_2 = \frac{I_g}{V_o}\cos(\phi_g) \quad (11a)$$

$$Y_v^i \delta V_1 - \frac{\partial(A'\sin\phi_2')}{\partial d}\delta d - \frac{\partial(A'\sin\phi_2')}{\partial\phi_2}\delta\phi_2 = \frac{I_g}{V_o}\sin(\phi_g) \quad (11b)$$

$$Y_v^r \delta V_2 - \frac{\partial(A\cos\phi_2'')}{\partial d}\delta d - \frac{\partial(A\cos\phi_2'')}{\partial\phi_2}\delta\phi_2 = 0 \quad (11c)$$

$$Y_v^i \delta V_2 - \frac{\partial(A\sin\phi_2'')}{\partial d}\delta d - \frac{\partial(A\sin\phi_2'')}{\partial\phi_2}\delta\phi_2 = 0 \quad (11d)$$

where all the derivatives are calculated at $d_{op}$ and $\phi_{2p}$, the symbol "$\delta$" is used to represent increments with respect to the free-running solution of the *coupled* system. Equations (11c) and (11d) are used to solve $\delta\phi_2$ in terms of $\delta d$, which provides a linear relationship $\delta\phi_2 = T(d_{op})\delta d$. The resulting expression is replaced in (11a) and (11b), and this leads to:

$$Y_v^r \delta V_1 + Q_r(d_{op})\delta d = \frac{I_g}{V_o}\cos(\phi_g)$$

$$Y_v^i \delta V_1 + Q_i(d_{op})\delta d = \frac{I_g}{V_o}\sin(\phi_g) \quad (12)$$

where the following terms have been introduced:

$$Q_r(d_{op}) = -A'\left[\frac{\cos(\phi_2 - \alpha)}{d} - \frac{\omega_s}{c}\sin(\phi_2 - \alpha)\right] + A'\sin(\phi_2')T(d_{op})$$

$$Q_i(d_{op}) = A'\left[\frac{\sin(\phi_2 - \alpha)}{d} + \frac{\omega_s}{c}\cos(\phi_2 - \alpha)\right] - A'\cos(\phi_2')T(d_{op}) \quad (13)$$

Squaring the two equations in (12), one can make $\cos(\phi_g)$ and $\sin(\phi_g)$ disappear. The resulting equation is:

$$\left|Y_v\right|^2 \delta V_1^2 + 2P_{vQ}\delta V_1\delta d + \left|Q\right|^2 \delta d^2 = \left(I_g / V_o\right)^2 \quad (14)$$

where $P_{vQ} = Y_v^r Q_r + Y_v^i Q_r$. Equation (14) corresponds to an ellipse in terms of $\delta V_1$ and $\delta d$, centered about $d_{op}$, $V_o + \Delta V_{op,1}$, where $\Delta V_{op,1}$ is the amplitude increment in (10), evaluated at $d_{op}$. Therefore, under low $I_g$, synchronization will be obtained in a sequence of distance intervals, located about $d_{op}$. From (12) it is derived that, at the limits of these intervals, the phase $\phi_g$ fulfils $\cos\left(\phi_g(d) - \alpha_v\right) = 0$.

The analysis method in (3) to (10) has been applied to a coupled oscillator system operating at 2.45 GHz. The individual oscillator is based on the transistor FET NE3210 and exhibits output power about 10 dBm [Fig. 1(b) and Fig. 1(c)]. The measurement setup is shown in Fig. 2. Each oscillator is connected to an antenna at the output port as shown in Fig. 1 (c). The peripheral oscillators are connected to directive antennas Siretta Oscar 18 which offer a 10 dB gain, and the central oscillator (node) is connected to an omnidirectional antenna with 5 dB gain. Due to space limitations in the laboratory, measurements have been performed for relatively small distances *d* (up to 2.2 m), which require a low antenna gain. Thus, suitable attenuators are connected between the oscillator output and the antenna, to keep the same EIRP. The output amplitudes are measured through the coupled port of a directional coupler connected between the antenna and the output port. The injection signal is provided by a Rohde & Schwarz SMT06 signal generator. For better insight, the injection signal is introduced into the central oscillator through its output port, which enables a direct application of the formulation presented. Introducing this source at a node different from the coupling node does not involve any analysis difficulties, since this is easily tackled through the methodology in [29]. However, the analytical expression would become

lengthy and less insightful. The input 50 Ohm resistor in Fig. 1(b) corresponds to the input impedance of a spectrum analyzer, used to easily detect the system status (synchronized or not) during each variation of the distance $d$.

The number of oscillator elements is $M = 4$. A small initial tuning was carried out, applied separately to each oscillator in free-running conditions (isolated from the coupled system). The length of the drain stub in Fig. 1(b) was slightly modified to obtain the same free-running frequency in all the oscillators.

Fig. 3 presents the variation of the system oscillation frequency (a) and amplitude (b) in free-running conditions, that is, in the absence of an input source, obtained by numerically solving system (10). In the considered distance range, from $d = 0.8$ m to 1 m, two steady-state solutions (in terms of $\omega_s$ and the two amplitudes $V_1$ and $V_2$) coexist for each distance value. These two coexisting solutions are denoted as Solution 1 and Solution 2. The free-running solution of the standalone oscillator is indicated in dotted line. The two frequencies at which the oscillator will be injection-locked at a later stage are marked in dashed line $f_{s1}$ and $f_{s2}$ in Fig. 3(a).

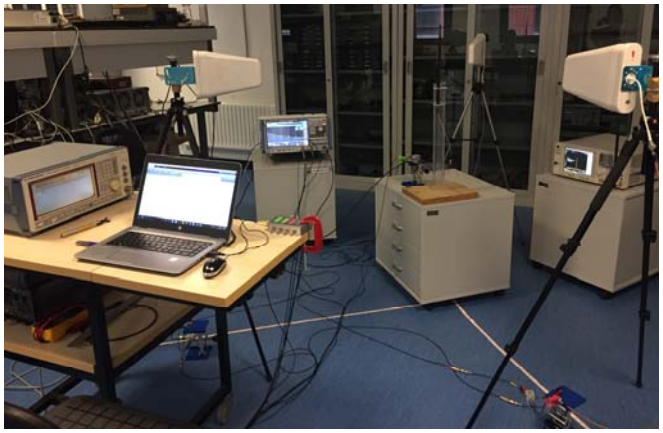

Fig. 2. Measurement setup. Each oscillator is connected to its antenna at the output port as shown in Fig. 1 (c). A spectrum analyzer (at the circuit input) is used in order to easily detect the system status at every distance variation. The output amplitudes are extracted through the coupled port of a directional coupler connected between the antenna and the output port. The injection signal is provided by a Rohde & Schwarz SMT06 signal generator.

Without an independent synchronization signal, the oscillation frequency of the coupled system exhibits minima and maxima about the individual-oscillator free-running frequency, given by $f_o = 2.4539$ GHz. The two steady-state solutions intersect at $f_o$, for which $\Delta\omega_s = 0$ in (10). As shown in Fig. 3(b), the amplitude $V_2$ of each of the two solutions also varies about the free-running value $V_o = 1.006$ V, whereas the amplitude $V_1$ of the first (second) solution exhibits a positive (negative) shift with respect to $V_o$ and a less pronounced variation with $d$. From a sufficiently large $d$, the coupling effects will be negligible and the two solutions will merge with the one corresponding to an isolated free-running oscillator ($f_o = 2.4539$ GHz, $V_o = 1.006$ V).

The results have been compared with those obtained through circuit-level HB simulations, represented in solid line, and with measurements, superimposed in Fig. 3(a). For the HB simulations, two AGs have been used [31]-[33], at the central and at the equivalent oscillator that represents any of the rest of system oscillators. The number of harmonic components is $NH = 8$. Note that the analytical formulation of the coupled system takes the harmonic content of the oscillator elements into account. This is because, in the finite-difference calculation of $Y_v$ and $Y_{\omega_s}$ a HB simulation is performed at each increment [20]-[22],[29]. As can be seen, the analytical formulation (10) exhibits an excellent agreement with the costly HB results. The highest discrepancies are obtained at the largest frequency and amplitude excursions, in consistency with the fact that (10) is based on a first-order approximation. The experimental characterization versus the distance $d$ was carried out by shifting the oscillators along the white lines shown in Fig. 2. Only stable solutions could be measured, and the results are superimposed in Fig. 3(a). As shown in the next subsection, Solution 2 is entirely unstable and Solution 1 is stable only in the intervals with negative slope of the curve in Fig. 3(a).

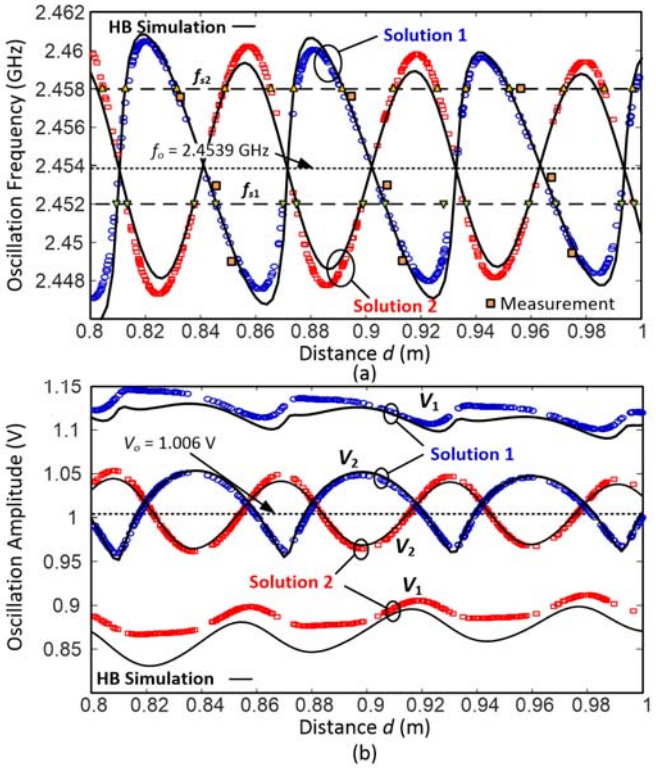


Fig. 3. Variation of the free-running solution of the star topology in Fig. 1 versus the distance $d$. There are two coexisting solutions (Solution 1 and Solution 2) in terms of $\omega_s$, $V_1$ and $V_2$. The free-running solution of the standalone oscillator is indicated in dotted line. HB simulations are represented in solid line. The two frequencies at which the oscillator will be injection-locked at a later stage are marked in dashed line. (a) Oscillation frequency, with measurements superimposed in the stable intervals. (b) Oscillation amplitude.

Fig. 4(a) presents the solution curves of the same system when introducing an independent synchronizing source into the middle oscillator. In this analysis, the source frequency is $f_s = 2.452$ GHz and its amplitude is $I_g = 1$ mA. For relatively small $I_g$, when increasing $d$, three regions with a distinct qualitative behavior are obtained. In the first region one obtains closed solution curves above and below the individual-oscillator free-running amplitude $V_o$, as shown in the expanded

view of Fig. 4(b). As $d$ increases, the curves in Fig. 4(a) merge into a single one (second region), shown in Fig. 4(c). Then, when further increasing $d$, they split into two curves with an oscillatory pattern (third region), shown in Fig. 4(d). The two oscillatory curves merge in a final turning point, which determines the maximum distance up to which synchronized steady-state solutions are possible. The higher the amplitude $I_g$, the smaller the distance from which the oscillatory pattern is obtained. Measurement points are superimposed in Fig. 4(b). These measurements were demanding, since stable synchronized solutions existed only in the small distance intervals corresponding to the upper side of the ellipsoidal curve $V_1$ (and its associated $V_2$ section).

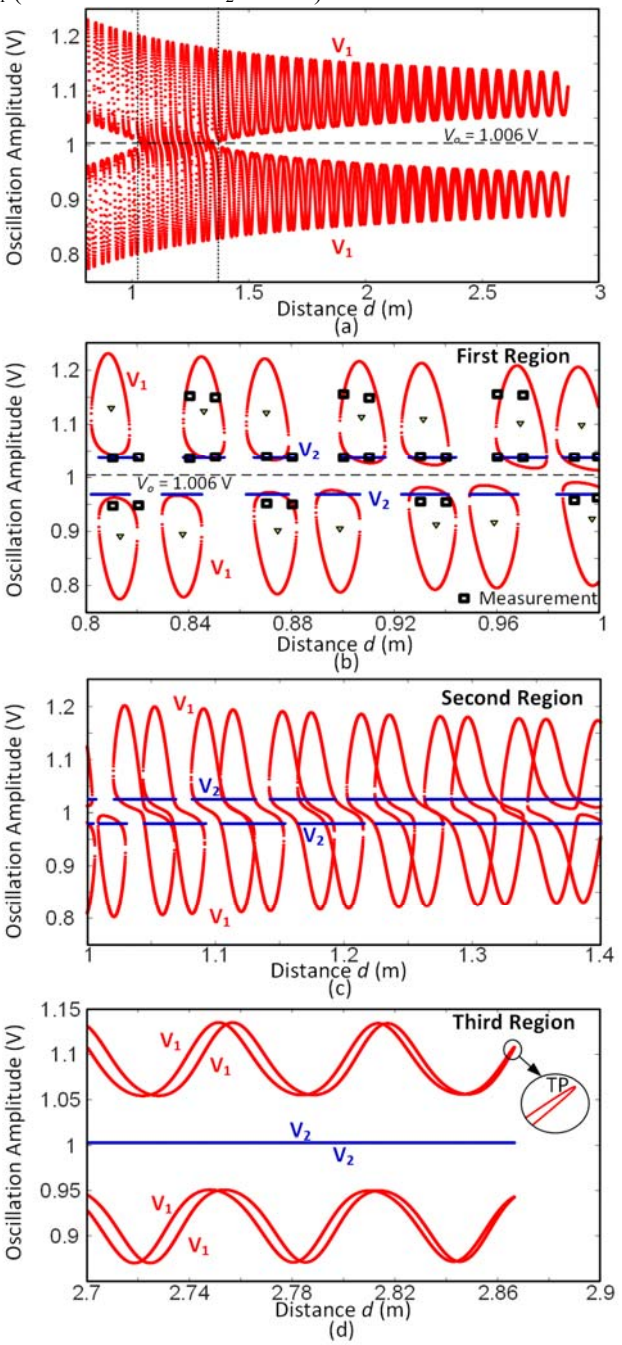


Fig. 4. Periodic solution curves of the system in Fig. 2. The source frequency is $f_s$ = 2.452 GHz and its amplitude is $I_g$ = 1 mA. Associated pairs of $V_1$, $V_2$ exhibit the same turning points. (a) Solution curves in the whole distance range. (b) First region with closed solution curves above and below the free-running frequency. Representative measurement points are superimposed. (b) Second region: the curves merge into a single one. (c) Third region: the curves with an oscillatory pattern merge in a final turning point.

In agreement with the theoretical results, the closed solution curves and the curve maxima are located about the distances $d_{op}$ at which the free-running frequency of the system [obtained from (10)] agrees with that of the synchronizing source. These free-running points are indicated with triangles in Fig. 4(b) and are located both above and below the free-running amplitude of the elementary oscillator, represented with a horizontal line. The solution curves are near-ellipsoidal in the case of the amplitude $V_1$ and nearly constant in the case of $V_2$. Associated pairs $V_1$, $V_2$ can be distinguished through inspection, as they exhibit the same turning points. When reducing $I_g$, the closed curves tend to the ellipses defined by (12).

The turning points of the solution curves can be obtained from the Jacobian of system (3). For compactness, the two following vectors are defined:

$$\bar{H} = \begin{bmatrix} H_1 & H_2 & H_3 & H_4 \end{bmatrix}^T$$
$$\bar{\mathrm{X}} = \begin{bmatrix} \Delta V_1 & \Delta V_2 & \Delta\phi_2 & \Delta\phi_g \end{bmatrix}^T \qquad (15)$$

As in any steady-state system [29]-[31], the Jacobian matrix of (3) becomes singular at the turning points, which fulfill:

$$\det\left[\frac{\partial \bar{H}}{\partial \bar{X}}\right] = Y_v^{i2}\sin(\phi_g)\sin(\phi_2^{"}) + Y_v^{r2}\cos(\phi_g)\cos(\phi_2^{"}) +$$
$$Y_v^i Y_v^r \sin(\phi_g + \phi_2^{"}) = 0 \qquad (16)$$

The evolution of the above determinant versus the distance $d$ is shown in Fig. 5. It passes through zero at all the turning points of the solution curves in Fig. 4(a). There are two different mechanisms causing these turning points, which are understood taking into account that the two equations (6) and (7) must provide real values of $\Delta V_2$ and $\Delta V_1$, respectively. The first mechanism to obtain a turning point is the zero value of the radicand (9). Its zeroes correspond to the turning points of the closed solution curves in Fig. 4(b) and Fig. 4(c), which are obtained when $I_g$ is small in comparison with $A'$. As the distance $d$ increases, the coupling coefficient $A'$ becomes smaller, so from a certain distance, the radicand (9) is always positive. The second mechanism for the occurrence of a turning point is the zero value of the radicand in (6), which determines the maximum distance ($d_{max}$) up to which synchronized steady-state solutions are possible. Making the radicand in (6) equal to zero and taking into account the definition of $A$ in (2), one obtains:

$$d_{\max} = \frac{c\sqrt{G_{tot}}}{\omega_s R_r |Y_\omega||\Delta\omega_s|\sin\alpha_{v\omega}} \qquad (17)$$

The above expression does not depend on the input current $I_g$ since for large distance $d$, the decrease of the coupling coefficient $A'$ ensures a positive value of the radicand (9).

Nevertheless, one must take into account that under too small *A'*, the coupling might be too weak for a robust operation. From inspection of (17), the distance $d_{max}$ decreases with the operation frequency $\omega_s$ and with the deviation with respect to the free-running oscillation frequency $|\Delta\omega_s|$. It would tend to infinite when injecting the system at the precise free-running oscillation frequency ($\Delta\omega_s = 0$), which is impossible in practice. On the other hand, $d_{max}$ increases with the antenna gain and depends on the particular oscillator design through $|Y_\omega|$ and the angle $\alpha_{v,\omega}$. In general, a stable individual oscillator design fulfils $\sin\alpha_{v,\omega} > 0$ [30], so it is not necessary to consider the absolute value of this sine function.

Fig. 6 presents a comparison between the curves obtained with the analytical formulation and with costly circuit-level HB simulations using two AGs. The HB simulations [Fig. 6(b)] were carried out setting the phase origin at one of the AGs and considering the AG amplitudes, the phase shift between the AGs and the input-source phase as state variables. Due to the complexity of the coexistent solution curves (Fig. 4), the only way to obtain these curves in HB was using the results of the analytical formulation [Fig. 6(a)], as an initial guess. Then, the HB solution curves were independently obtained through AG optimization and manual parameter switching [33].

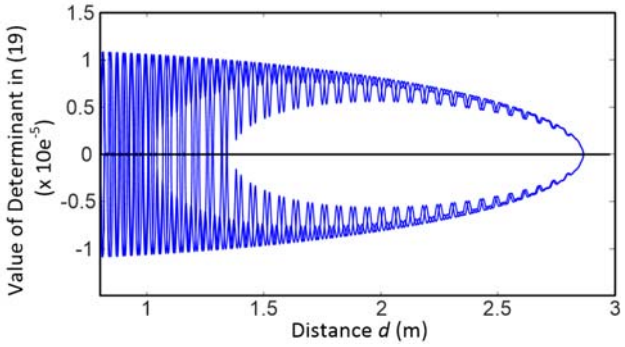


Fig. 5. Turning point mechanism. Variation of the determinant in (16) versus the distance *d* between the central oscillator and the peripheral oscillators.

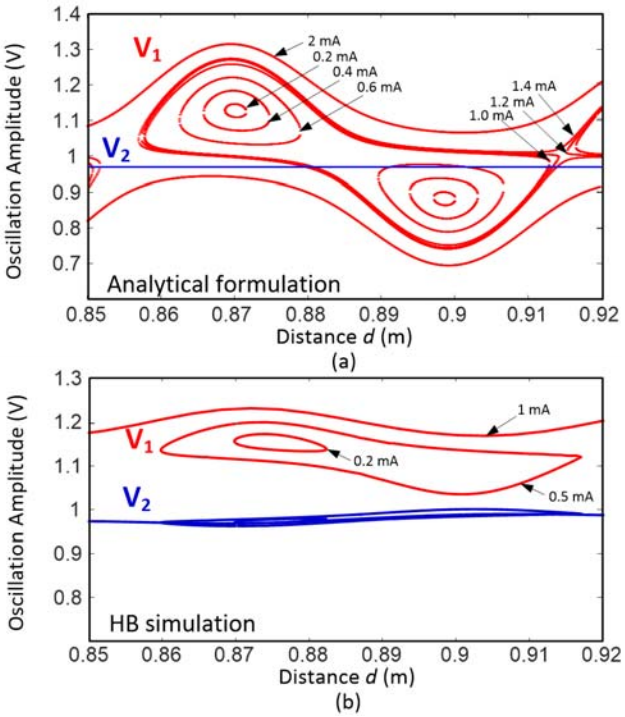


Fig. 6 Comparison of the amplitude curves obtained with the analytical formulation and with costly circuit-level HB simulations using two AGs. (a) Results of the analytical formulation. (b) HB results using AG optimization and manual parameter switching.

The HB simulations were extremely lengthy and demanding. This is why only three $I_g$ values and only some solution curves are shown in Fig. 6(b). There is a good qualitative agreement, though the first-order approximation in (3), neglecting, for instance, $V_o+\Delta V_1$ in the denominator of the $I_g$ term, leads to certain error in the amplitude predictions. This could be easily circumvented with a higher-order approach, solving the resulting formulation numerically. The error decreases when increasing the distance *d*, since the amplitude deviations become smaller (see Fig. 4).

The spectra measured in the central oscillator and one representative peripheral oscillator, for $I_g = 2$ mA and $d =$ 0.85 m, are shown in Fig. 7, where they can be compared with the analytical and HB-simulation results. A 10 dB coupler has been used to extract the output power, what explains the difference of about 10 dB with respect to the simulations. No spurious components are present. The synchronized steady-state solution is robust with a high stability margin.

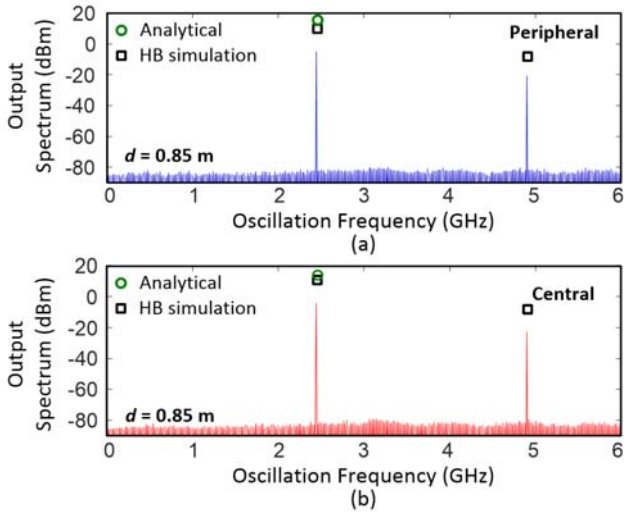


Fig. 7. Spectra measured in the central oscillator (a) and one representative peripheral oscillator (b), for $I_g = 2$ mA and $d = 0.85$ m. The experimental spectra can be compared with the analytical and HB results. A 10 dB coupler has been used to extract the output power, what explains the level differences.

### *B. Generalization to an arbitrary topology*

In case the $M$–1 oscillators are both coupled to the injected one (Osc. 1) and among themselves, the system solution curves will be qualitatively similar to the ones in Fig. 4. The analysis will simplify if the system topology is symmetric and the injection-locked oscillator is also symmetrically located with respect to the other elements (above or below). Then, the system equations are the following:

$$Y(V_c,\omega_s)V_c e^{j\phi_c} = C_L\ V_1 + C_L\ V_2 e^{j\phi_2} + \ldots + C_L\ V_N e^{j\phi_N} + I_g e^{j\phi_g} \quad (18a)$$

$$\left[Y(\bar{V},\omega_s)\right]\bar{V}_s = [C]\bar{V}_s + [C_L]_d V_c e^{j\phi_c} \quad (18b)$$

where $V_c, \phi_c$ are, respectively, the amplitude and phase of the central oscillator (containing the injection source) and $V_i, \phi_i$, with $i = 2 \ldots M$, are the amplitudes and phases of the rest of oscillators, having an arbitrary symmetric topology, such as those considered in [14]-[15]. On the other hand, $[C]$ is the coupling matrix, which depends on the topology of the 2 to $M$ oscillators, $\bar{V}_s$ is the vector composed by the complex voltages of these oscillators at the antenna nodes and $[C_L]_d$ is a diagonal matrix having equal elements $C_L$.

In globally-coupled symmetric topologies [14]-[15], the matrix $[C]$ is circulant [34]. In the case of $M$–1 oscillators, its eigenvalues $\lambda_n$ and eigenvectors $\bar{V}_{s,n}$ have the form:

$$\bar{V}_{s,m} = \frac{V_o}{\sqrt{M-1}}\left(1\ \ e^{j\frac{m2\pi}{M-1}}\ \ e^{j\frac{2m2\pi}{M-1}}\ \ldots\ e^{j\frac{(M-2)2\pi}{M-1}}\right)^T \quad (19)$$

The eigenvalues $\lambda_n$ depend on the system topology and number of elements $M$–1. Taking into account the diagonal quality of $[C_L]_d$, one can apply the above eigenvalue analysis to (18b), which provides:

$$Y_v^r\ \Delta V_c + Y_\omega^r \Delta\omega_s = C_L\ e^{-j\phi_c} + C_L\ e^{j\phi_2-\phi_c} + \ldots + C_L\ e^{j\phi_N-\phi_c} + \frac{I_g}{V_o} e^{j\phi_g-\phi_c} \quad (20a)$$

$$Y_v^r\ \Delta V_p + Y_\omega^r \Delta\omega_s = \zeta(m,M-1)C_L + C_L e^{j\phi_c} \quad (20b)$$

where $\Delta V_c, \Delta V_p$ are amplitude increments with respect to $V_o$ of the central and peripheral oscillators, respectively, $\lambda_m = \zeta(m,M-1)C_L$ is each of $M$–1 eigenvalues of the coupling matrix $[C]$, $\phi_2, \phi_3 \ldots \phi_N$ are the phases of the components of (19) and second-order terms have been neglected. From inspection of (20), one has a system with the same qualitative form as (3). At a fixed input frequency $\omega_s$, the complex equation (20b) can be solved for $\Delta V_p, \phi_c$. Then, equation (20a) can be solved for $\Delta V_c, \phi_g$. The procedure is identical to the one applied in (3). However, the analysis of (20) requires considering all the possible oscillation modes of the coupled system [14]-[15].

Fig. 8 shows the measured spectra of the peripheral and central oscillators when replacing the directive antennas in the peripheral oscillators with omnidirectional ones. A stable and highly robust behavior is also obtained in this case.

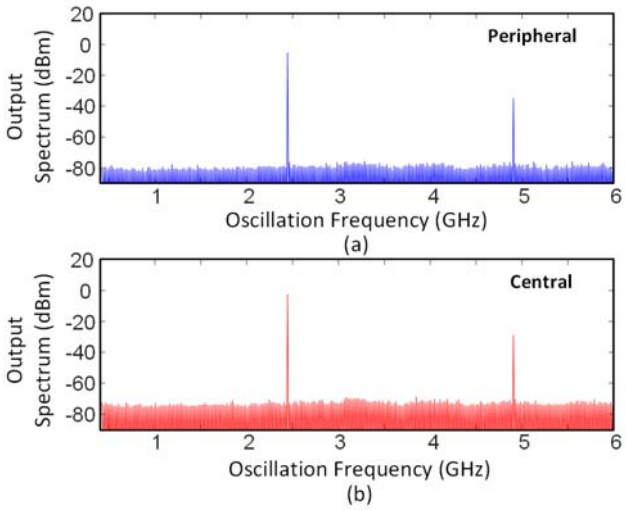


Fig. 8. Spectra measured in the central oscillator (a) and one representative peripheral oscillator (b), for $I_g = 2$ mA and $d = 0.85$ m, when replacing the directive antennas in the peripheral oscillators with omnidirectional ones.

In arbitrary configurations, even if the antenna of the oscillator (Osc. 1) injected by the independent source at $\omega_s$ cannot reach a set of oscillators, a global synchronization of the whole system to $\omega_s$ is possible. This is because the oscillators in shadow are coupled to oscillators that are, in turn, coupled to Osc. 1. The behavior is analogous to the one in nearest-neighbor coupled oscillators for beam-steering applications [17]-[22], where the injection signal is introduced, in most cases, in one of the oscillators only.

### C. Stability

The stability analysis is essential in the presence of several coexistent solutions. A small perturbation is considered, which gives rise to small increments in all the oscillator amplitudes and phases, represented as $\delta V_{s,m}(t)$, $\delta\phi_{s,m}(t)$, where $m = 1$ to $M$. These perturbations will be different in the various oscillator elements, so it will not be possible to use the reduced two-element equivalent system (1) for the stability analysis. The same will be true for the noise analysis addressed in the next subsection. On the other hand, the perturbed frequency becomes $j\omega_s+s$ [30], [33]. Due to the small value of the perturbations, it is possible to perform a first-order Taylor series expansion of the coupled system about each steady-state solution. The complex-frequency increment $s$ acts like a time differentiator, which gives rise to terms of the form $\delta\dot{\phi}_m - j\delta\dot{V}_m / V_o$ [30], [33]. Thus, one obtains the following LTI differential system:

$$\begin{aligned}
&\left\{\left[\frac{\partial Y(\bar{V}_s,\omega_s)}{\partial \bar{V}}\right]\left[V_{s,m}e^{j\phi_{s,m}}\right]_d\right\}\delta\bar{V}_s(t)+\\
&\left\{\left\{\left[Y(\bar{V}_s,\omega_s)\right]-[C]\right\}\left[jV_{s,m}e^{j\phi_{s,m}}\right]_d+\left[\frac{\partial H}{\partial\phi_g}\right]\right\}\delta\bar{\phi}_s(t)+\\
&\left\{\left[\frac{\partial Y(\bar{V}_s,\omega_s)}{\partial j\omega}\right]-\left[\frac{\partial C(\omega_s)}{\partial j\omega}\right]\right\}\left[V_{s,m}e^{j\phi_{s,m}}\right]_d\\
&\left[\frac{1}{V_{s,m}}\delta\dot{V}_{s,m}(t)+j\delta\dot{\phi}_{s,m}(t)\right]_v=0
\end{aligned}\tag{21}$$

where the subscript $d$ indicates a diagonal matrix, the subscript $v$ indicates a column vector and the following matrixes have been introduced (21):

$$[C]=\begin{bmatrix}0 & Ae^{-j\alpha} & \dots & Ae^{-j\alpha}\\ Ae^{-j\alpha} & 0 & \dots & 0\\ \vdots & \vdots & \vdots & \vdots\\ Ae^{-j\alpha} & 0 & \cdots & 0\end{bmatrix},\left[\frac{\partial H}{\partial\phi_g}\right]=\begin{bmatrix}j\frac{I_g}{V_o} & 0 & \dots & 0\\ 0 & 0 & \dots & 0\\ \vdots & \vdots & \vdots & \vdots\\ 0 & 0 & \cdots & 0\end{bmatrix}\tag{22}$$

The matrix $[\partial H/\partial\phi_g]$ accounts for the effect of the synchronizing source on the stability properties. One should note that the matrix equation (21) is of general application to wireless-coupled systems with arbitrary topology, under external injection. Splitting (21) into real and imaginary parts, one obtains the following compact system, of $2M$ dimension:

$$[M_1]\begin{bmatrix}\delta\dot{V}_1(t)\\ \vdots\\ \delta\dot{V}_N(t)\\ \delta\dot{\phi}_1(t)\\ \vdots\\ \delta\dot{\phi}_M(t)\end{bmatrix}-[M_2]\begin{bmatrix}\delta V_1(t)\\ \vdots\\ \delta V_N(t)\\ \delta\phi_1(t)\\ \vdots\\ \delta\phi_M(t)\end{bmatrix}=0\tag{23}$$

where the real-element matrixes $[M_1]$ and $[M_2]$ are directly extracted from (21). In fact, it is straightforward to demonstrate that the matrix $[M_2]$ agrees with the Jacobian in $\partial\bar{H}/\partial\bar{X}$. The stability is analyzed by calculating the $2M$ eigenvalues associated with system (23).

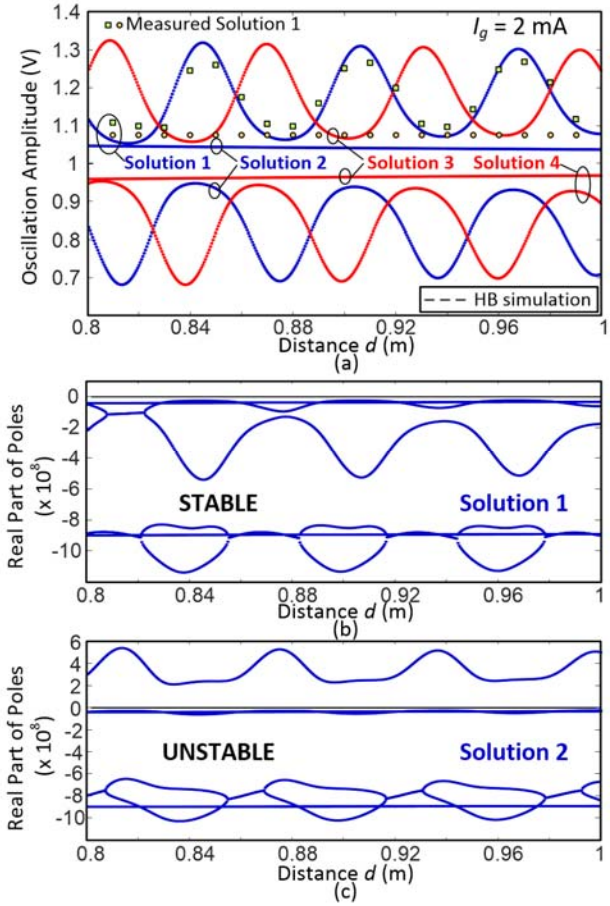


Fig. 9. Stability analysis for $I_g$ = 2 mA, in the distance interval 0.8 m to 1 m. (a) Coexisting steady-state solutions. (b) Stability analysis of Solution 1 (stable). The real part of the poles has been represented versus $d$. (c) Stability analysis of Solution 2 (unstable).

In a first investigation, a generator amplitude $I_g$ = 2 mA has been considered in the coupled system of Fig. 1. The distance interval analyzed is 0.8 m to 1 m. For this $I_g$ value, the solution curves are oscillatory, as shown in Fig. 9(a), though the system is still far from the final turning point. The four coexisting solutions are shown in Fig. 9(a). Each solution has its own stability properties, determined by its corresponding $2M = 8$ poles. Unlike the situation in a coupled system in free-running conditions [14]-[15], there is no real pole permanently at zero for all the $d$ values, since the system is non-autonomous. All the

poles of Solution 1, shown in Fig. 9(b), have a negative real part, so this solution is stable in the whole distance interval. In contrast, Solution 2, 3 and 4 are unstable in the whole interval. Therefore, there will be no problems of physical coexistence of distinct solutions. As an example, Fig. 9(c) shows the real part of the poles of Solution 2. Measurements are superimposed on the stable Solution 1.

The stability properties of the coupled system with an injection-locking source have been compared with those in free-running conditions. Fig. 10 presents the dominant poles of the two free-running solutions coexisting in the distance interval 0.8 m to 1 m, shown in Fig. 3. In each case, the real part of the poles has been represented versus $d$. Solution 1 is stable only in some distance intervals [Fig. 10(a)], whereas Solution 2 is always unstable [Fig. 10(b)]. From the comparison of Fig. 9(b) and Fig. 10(a), the injection-locking source is able to stabilize the coupled solution in the whole distance interval, enhancing the system robustness. This is a relevant result since the main drawback of the wireless-coupled system in free-running conditions is the alternation of the stable and unstable operation intervals [14]-[15].

The next objective is to analyse the influence of the injection amplitude $I_g$ and the antenna gain on the stability properties. The input frequency is set to $f_s$ = 2.4539 GHz and the distance is set to a relatively high value $d$ = 2.5 m, near the operation boundaries detected in Fig. 5. Fig. 11 presents the variation of the steady-state solutions versus the antenna gain $G$, for two $I_g$ values. Increasing $I_g$, synchronized solutions are obtained up to a higher $G$ value, as can be seen by comparing the results of Fig. 11(a), for $I_g$ = 2 mA, and Fig. 11(b), for $I_g$ = 5 mA. Solution 1 and Solution 2 respectively correspond to the upper and lower section of the curve in darker solid line. Solution 3 and Solution 4 respectively correspond to the upper and lower section of the curve in lighter solid line. As shown next, for the two $I_g$ values, only Solution 1 is stable, in a certain $G$ interval.

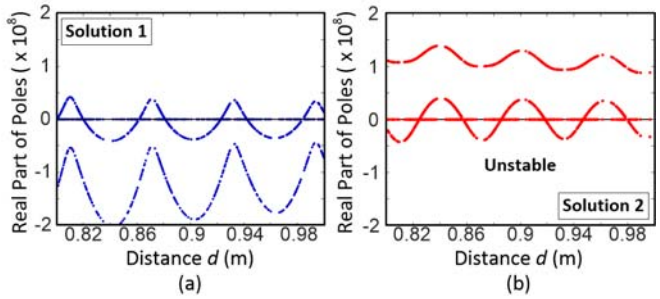


Fig. 10. Stability analysis of the two free-running solutions of the coupled system, shown in Fig. 2. The real part of the dominant poles has been represented versus $d$. (a) Solution 1. (b) Solution 2.

Fig. 12 shows the evolution of the real part of dominant poles of Solution 1 versus $G$. For the lower amplitude $I_g$ = 2 mA [Fig. 12(a)], the solution curve is stable until the turning point $T$, where a real pole crosses through zero, in agreement with the infinite slope of the solution curve. This real pole is on the right-hand side of the complex plane in Solution 2. In injection-locked oscillators with small injection power, turning points are generally associated to desynchronization [35]-[36]. The oscillation unlocks from the input source and gives rise to a quasi-periodic solution. The offset between the source and oscillation frequencies departs from zero at the bifurcation point [35], which causes a very dense spectrum in the neighborhood of this bifurcation. An example will be shown in Subsection II.E.

For the higher amplitude $I_g$ = 5 mA [Fig. 11(b)], the turning point $T$ occurs at a higher $G$ value. However, Solution 1 is not stable up to the point $T$. When increasing $G$, the stronger coupling effects (higher $A$) lead to desynchronization through a direct Hopf bifurcation [37]-[38], indicated in Fig. 11(b) and Fig. 12(b). At this bifurcation, a pair of complex-conjugate poles cross through the imaginary axis to the right hand side of the complex plane (RHS), so the coupled system becomes unstable. At the Hopf bifurcation, a new fundamental frequency arises (associated with the unlocked oscillation), in addition to $\omega_s$, which also gives rise to a transition to quasi-periodic regime. Unlike what happens at turning points, it arises from zero amplitude and the generated spectral lines are relatively sparse.

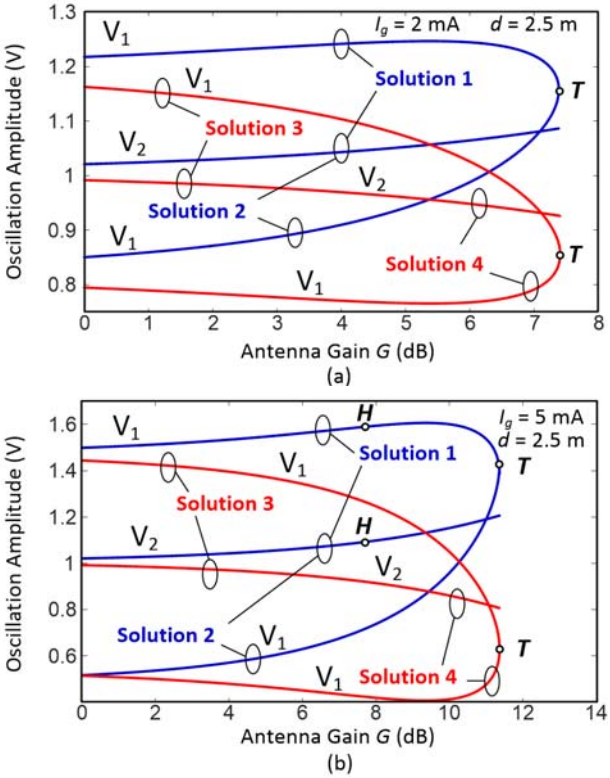


Fig. 11. Variation of the steady-state solutions versus the antenna gain $G$, for two $I_g$ amplitudes, at $f_s$ = 2.4539 GHz and $d$ = 2.5 m. (a) $I_g$ = 2 mA. (b) $I_g$ = 5 mA. The Hopf bifurcation point is indicated with "$H$".

## D. Phase noise

For the phase-noise analysis, an equivalent current noise source $I_{N,m}$, where $m$ = 1 to $M$, is connected to each oscillator, at its corresponding antenna node. This equivalent source is calculated as indicated in [39]. The set of individual-oscillator noise sources composes the vector $\overline{I}_N(t)$. Regarding the injection source, its amplitude noise is neglected and only its phase noise $\psi(t)$ is considered. In synchronized conditions, the phase perturbations of each oscillator ($m$ = 1 to $M$) will be the addition of $\psi(t)$, directly transferred to all the oscillators, and $\delta\phi_m(t)$, associated with the perturbation of the oscillator voltage

phasor [33], [39]-[40]. Thus, the total phase perturbations of the $M$ oscillators are given by:

$$\delta\phi_1(t)+\psi(t),\delta\phi_2(t)+\psi(t)\ldots,\delta\phi_N(t)+\psi(t) \qquad (24)$$

On the other hand, the multiplication by the time differentiator $s$, arising from the frequency increment, will give rise to terms of the form:

$$\left(\dot{\psi}+\delta\dot{\phi}_m\right)-j\delta\dot{V}_m/V_o \qquad (25)$$

Thus, the noisy system is governed by the following matrix system:

$$\left[M_1\right]\begin{bmatrix}\delta\dot{V}_1(t)\\ \vdots\\ \delta\dot{V}_m(t)\\ \delta\dot{\phi}_1(t)+\delta\dot{\psi}\\ \vdots\\ \delta\dot{\phi}_M(t)+\delta\dot{\psi}\end{bmatrix}=\left[M_2\right]\begin{bmatrix}\delta V_1(t)\\ \vdots\\ \delta V_M(t)\\ \delta\phi_1(t)\\ \vdots\\ \delta\phi_M(t)\end{bmatrix}+\begin{bmatrix}I^r_{N,1}(t)\\ \vdots\\ I^r_{N,M}(t)\\ I^i_{N,m}(t)\\ \vdots\\ I^i_{N,M}(t)\end{bmatrix} \qquad (26)$$

For compactness, a state-variable vector $\delta\bar{x}(t)$ is defined:

$$\delta\bar{x}(t)=\left[\delta V_1(t)\ \ \ldots\ \ \delta V_N(t)\ \ \delta\phi_1(t)\ \ \ldots\ \ \delta\phi_M(t)\right]^T \qquad (27)$$

Applying the Fourier transform to (26), one obtains:

$$\left\{\left[M_1\right]j\Omega-\left[M_2\right]\right\}\delta\bar{x}(\Omega)=\bar{I}_N-\left[M_1\right]j\Omega\ \bar{\psi}(\Omega) \qquad (28)$$

where the following vector has been introduced:

$$\delta\bar{\psi}(t)=\left[0\ \ \ldots\ \ 0\ \ \delta\psi(\Omega)\ \ \ldots\ \ \delta\psi(\Omega)\right]^T \qquad (29)$$

The phase noise at a given oscillator $m$ is $\delta\phi_{m,T}(\Omega)=\delta\phi_m(\Omega)+\psi(\Omega)$, which is obtained by solving (28) for $\delta\phi_m(\Omega)$. Then, the phase-noise spectral density at the oscillator $m$ is obtained by multiplying the result by $\delta\phi^*_{m,T}(\Omega)$, taking into account that the oscillator noise sources $I_{N,m}$(t) and the phase noise $\psi(t)$ of the injection source are uncorrelated.

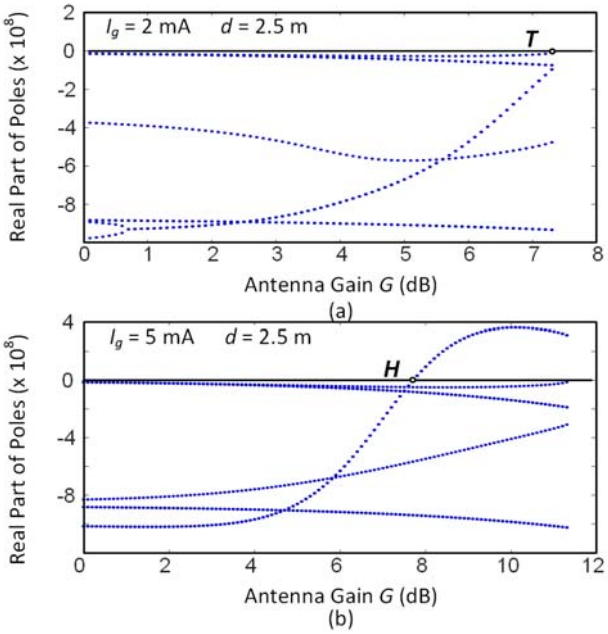


Fig. 12. Evolution of the real part of dominant poles of Solution 1 versus $G$, for two amplitudes $I_g$ of the synchronizing source. (a) $I_g$ = 2 mA. The solution curve is stable up to the turning point $T$, in Fig. 12(a). (b) $I_g$ = 5 mA, the solution is stable up to the Hopf bifurcation point, indicated with "$H$".

Fig. 13 compares the phase-noise behavior of the coupled system in free-running conditions and under an injection signal of amplitude $I_g$ = 2 mA, at the distance $d$ = 0.85 m for two different values of the input frequency $f_s$, in the middle of the synchronization band and near the band limit. In the two cases, the spectra corresponding to the central oscillator and a representative peripheral oscillator have been represented. The spectrum corresponding to the standalone free-running oscillator is also shown, as a reference. In all cases, there is an excellent agreement with the experimental results, obtained with the equipment R&S FSWP phase noise analyser.

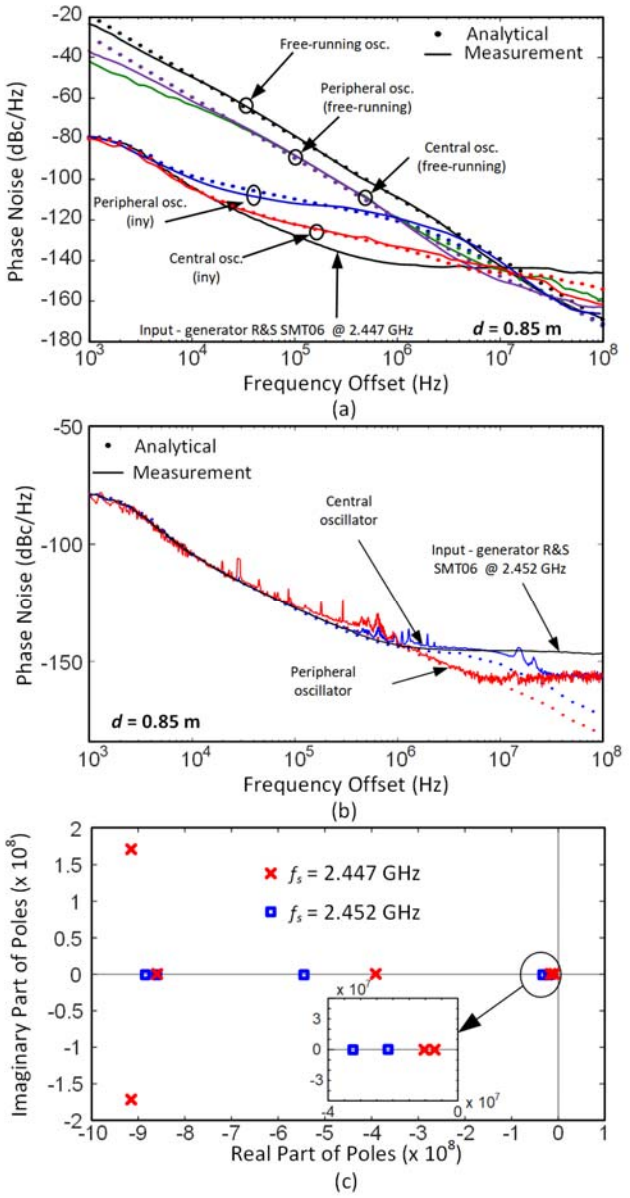


Fig. 13. Phase noise of the coupled system at $d = 0.85$ m. (a) $f_s = 2.447$ GHz, near the edge of the synchronization band. Comparison of the phase-noise spectrum of the coupled system obtained in free-running conditions and under $I_g = 2$ mA. The spectrum of the standalone free-running oscillator is also shown, as a reference. The measured spectra are represented in solid line. (b) $f_s = 2.452$ GHz, under a sufficient stability margin. (c) Pole locus at $f_s = 2.447$ GHz (red crosses) and $f_s = 2.452$ GHz (squares). Inset: Expanded view.

Both the phase noise of the central and the peripheral oscillator follow the phase-noise spectral density of the input source at low offset frequencies and tend to the spectral density of the free-running oscillator as the offset frequency increases. In the intermediate offset-frequency interval, the phase noise of the central oscillator is lower than that of the peripheral one, due to strongest impact of the input source, connected to this oscillator. In Fig. 13(a), the system purposely operates under a small stability margin, with $f_s = 2.447$ GHz, near the synchronization boundary. This is to demonstrate that the formulation (24) to (28) can accurately predict the noise amplification due a small stability margin, which, in the peripheral oscillator, gives rise to a relatively high plateau in the intermediate range of offset frequencies. When choosing $f_s = 2.452$ GHz, to operate relatively far from the synchronization boundaries, the phase-noise spectral density decreases as shown in Fig. 13(b).

Fig. 13(c) compares the stability properties for the two injection frequencies $f_s = 2.447$ GHz and $f_s = 2.452$ GHz. In the two cases, the dominant poles are real. In consistency with the phase noise analysis, the stability margin is smaller for $f_s = 2.447$ GHz (see expanded view in the inset). Under this small stability margin, there is a noise amplification effect, without resonance peaks, since the effect is caused by real poles, instead of complex-conjugate poles [41].

### *E. Synchronization bandwidth and scaling with distance*

As derived in Subsection II.A, the existence of a periodic oscillatory solution at the frequency of the independent source $\omega_s$ requires the fulfilment of the two following conditions:

$$A^2 - |Y_\omega|^2 \Delta\omega_s^2 \sin^2 \alpha_{v\omega} > 0 \tag{30a}$$

$$\begin{aligned}&(I_g / V_o)^2 - A'^2 \sin^2(\phi_2' - \alpha_{v\omega}) + \\ &2A'|Y_\omega|\Delta\omega_s\left(\cos(\alpha_{v\omega}) - 1\right)\cos(\phi_2' - \alpha_{v\omega}) \\ &-|Y_\omega|^2 \sin^2 \alpha_{v\omega} \Delta\omega_s^2 > 0\end{aligned} \tag{30b}$$

Both $A$ and $A'$ are inversely proportional to $d$, so from certain $I_g$ value ($I_{gmin}$), condition (30b) will always be fulfilled. Therefore, for $I_g > I_{gmin}$, the synchronization bandwidth will be solely determined by condition (30b). Equating the term on the left-hand side to zero, taking into account the two opposed signs of the square root and making use of the definition of $A$ in (2) the synchronization bandwidth ($\omega_{s1}$, $\omega_{s2}$) is given by:

$$\begin{aligned}\omega_{s1} &= \frac{\omega_o}{2} + \sqrt{\left(\frac{\omega_o}{2}\right)^2 - \frac{c\sqrt{G_{tot}}}{|Y_\omega| R_r d \sin\alpha_{v\omega}}} \\ \omega_{s2} &= \frac{\omega_o}{2} + \sqrt{\left(\frac{\omega_o}{2}\right)^2 + \frac{c\sqrt{G_{tot}}}{|Y_\omega| R_r d \sin\alpha_{v\omega}}}\end{aligned} \tag{31}$$

As gathered from (31), the synchronization bandwidth decreases with $d$, which can be compensated with a larger antenna gain. The value of $I_{gmin}$ is easily determined using (31) to solve for $\phi_2'$ from 3(c) and 3(d). For $I_g > I_{gmin}$ the injection current $I_g$ does not affect the synchronization bandwidth. However, it has a substantial effect on the stability properties. In the ranges of validity of our model, the stability margin increases with $I_g$. In the experiment, we have not observed any destabilization when increasing the injection power up to 16 dBm, which is the maximum provided by the Rohde & Schwarz SMT06 signal generator.

Fig. 14(a) shows the synchronized solutions obtained at $d = 2.2$ m, traced in terms of $V_1$ versus $f_s$, for different $I_g$ values. For each $I_g$, they compose two closed curves, represented with the same color. In agreement with the analytical derivation, the injection current does not affect the synchronization bandwidth. However, it affects $V_1$, as gathered from Fig. 14(a) and 3(a)-(b). Fig. 14(b) shows the variation of the real part of the poles of the

Solution 1 denoted as $S_1$ (comprised between the two turning points) versus $f_s$. The other three coexisting solutions are unstable. Increasing $I_g$ there is an increase of the stability margin. Measurement points corresponding to the solution $S_1$ are superimposed in Fig. 14(a). Fig. 14(c) shows the spectrum measured immediately after unlocking. Its density is consistent with the system destabilization due to a turning point.

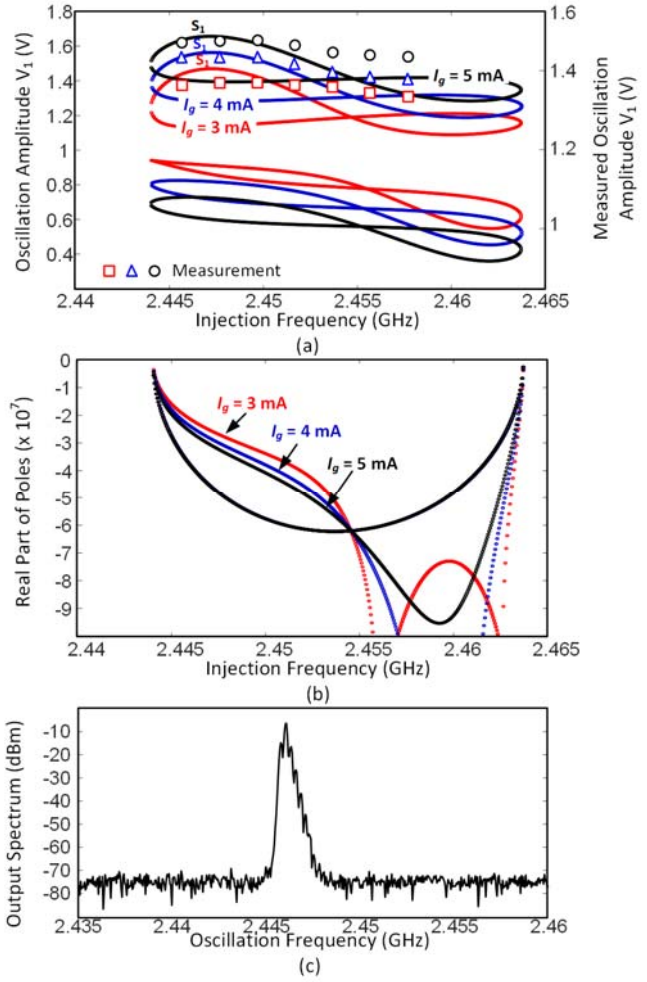


Fig. 14 Synchronized solutions obtained at $d = 2.2$ m with 3 dB antenna gain. (a) Solution curves traced in terms of $V_1$ versus $f_s$, for different $I_g$ values (b) Variation of the real part of the poles of the solution denoted as $S_1$ versus $f_s$. (c) Spectrum measured just after destabilization.

Fig. 15 presents an analysis of the variation of the locking bandwidth with the distance $d$, for fixed antenna gain is 3.5 dB and $I_g = 3$ mA. In Fig. 15(a), the synchronized solutions have been traced in terms of $V_1$ versus $f_s$, for $d = 5$ m, 10 m and 15 m. The locking bandwidths are 12 MHz, 6 MHz and 4 MHz, respectively. In all the synchronization curves, the solution $S_1$ (comprised between the two turning points) is stable. Fig. 15(b) shows the variation of the real part of the dominant poles of $S_1$ with the injection frequency $f_s$, for the three $d$ values. As expected, there is a reduction of both the locking bandwidth and the stability margin when the distance increases. Nevertheless, the system seems capable to operate at larger distances $d$, which, as gathered from (31), requires higher antenna gain, for a sufficient frequency bandwidth, and higher injection amplitude, for a sufficient stability margin.

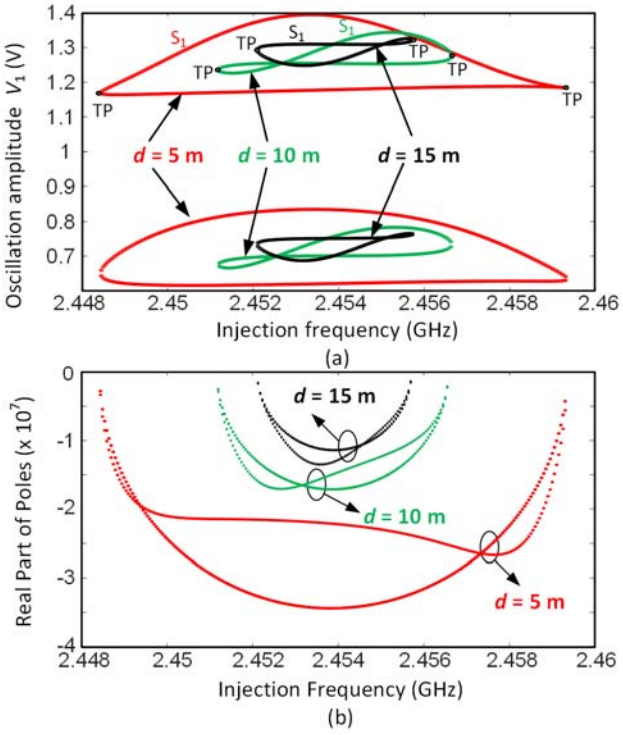


Fig. 15 Variations of the locking bandwidth (in terms of $f_s$) with the distance $d$. (a) Oscillation amplitude $V_1$ versus $f_s$ for $d = 5$ m, 10 m and 15 m. (b) Variation of the real part of the dominant poles of the solution $S_1$ versus $f_s$, for the three $d$ values.

### *F. Effect of interference signals*

The effect of interference signals on the behavior of the coupled system will depend on their power and frequencies. Under low power interferers, the system will maintain its synchronized periodic state at $\omega_s$ and there will simply be a mixing with the interferer frequencies. However, stronger interferers can induce unlocking through either a desynchronization turning point or a Hopf bifurcation of the mixer-like solution [42]-[44]. This may happen in one or more oscillators and will lead to a spectrum containing one or more additional fundamental frequencies, resulting from the unlocking of one or more oscillators. The power required to induce the unlocking will be generally smaller for a smaller difference between the interferer frequency and $\omega_s$, due to an increase in the system sensitivity near the synchronization band.

In order to quantify the system robustness to interference effects, both numerical simulations and measurements have been carried out. The numerical simulations are based on the envelope-transient method [45]-[47], representing the oscillator signals in a Fourier series with slowly-varying harmonic terms $\bar{x}(t) = \sum_k \bar{X}_k e^{jk\omega_s t}$. The injection amplitude and frequency are $I_g = 1$ mA and $f_s = 2.45$ GHz, respectively. In the experiment, the interference source is closer to the central oscillator than the peripheral oscillators, so different interferer-current amplitudes $I_{int}$ and $\alpha I_{int}$, where $\alpha$ is a scaling factor, are considered. The factor $\alpha$ accounts from the propagation loss, so the dominant interference effect is the one undergone by the central oscillator. The interferer frequency is $f_{int} = 2.5$ GHz. Fig. 16

presents a comparison of the simulated and measured spectra in the central and peripheral oscillators for different values of $I_{int}$. Simulated and measured spectra without an interference ($I_{int}$ = 0 mA) are shown in Fig. 16(a) and (b), for a comparison reference. Simulated and measured spectra for $I_{int}$ = 1 mA are shown in Fig. 16(c) and (d). The system remains locked but there is a mixing effect. Finally, simulated and measured spectra for $I_{int}$ = 4 mA are shown in Fig. 16(e) and (f). A new fundamental frequency, at small offset from $f_s$, can be noted, which is due to the oscillation unlocking with respect to the input source. Taking into account the low $I_g$ value, the system can be considered rather robust versus interference effects.

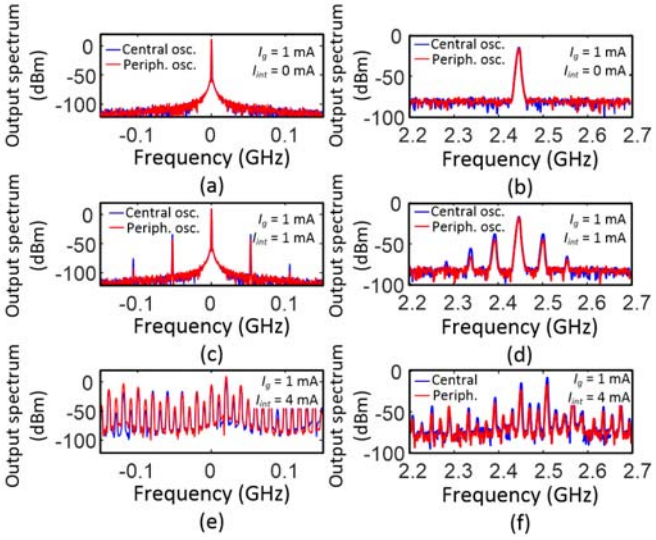


Fig. 16 Comparison of the simulated [(a), (c), (e)] and measured spectra [(b), (d), (f)] in the central and peripheral oscillators for different values of $I_{int}$. (a) and (b) $I_{int}$ = 0 mA. (c) and (d), $I_{int}$ = 1 mA. (e) and (f), $I_{int}$ = 4 mA. Unlocked.

### G. *Numerical analysis of the time response*

The system time response when an oscillator is powered on and off has been analyzed with the envelope-transient method [45]-[47]. The oscillator is powered off by setting its drain bias voltage to $V_D$ = 0 V instead of the nominal value $V_D$ = 2.5 V. In the simulation, one of the three surrounding oscillators is powered off from $t_{off}$ = 20 ns to $t_{on}$ = 50 ns. At the latter time, this oscillator is powered on again. Fig. 17(a) shows the evolution of the amplitude of the first harmonic component of the voltage signal $V_{1,1}(t)$ at the output of each of the four oscillator circuits from the initial time $t$ = 0 ns to 100 ns. The start-up transient can be noted and leads to a steady-state solution having slightly larger amplitude in the central oscillator than in the three peripheral oscillators, which, as expected, exhibit overlapped waveforms. At $t_{off}$ = 20 ns, the drain bias voltage of one of the peripheral oscillators is shifted from 2.5 V to 0 V. At $t_{on}$ = 50 ns, this drain bias is shifted from 0 V to 2.5 V. Note that the switching of this oscillator gives rise to a transient in all the rest of oscillator elements, as expected due to the coupled operation of the system. Fig. 17(b) and (c) show the measurements carried out using a BB60C Real-time Spectrum Analyzer/ RF recorder from Signal Hound in a zero-span mode. The bias source that is turned on and off is an E36312A power supply from Keysight, which has a time response of 45 ms. This explains the difference with the simulations. The output signal is extracted through a 10 dB coupler. Fig. 17(b) shows the effect of switching *off* and *on* a peripheral oscillator, on the central oscillator, and Fig. 17(c) shows the effect on one of the other peripheral oscillators. The switch off and on times do not agree since the measurements were carried out in sequential experiments.

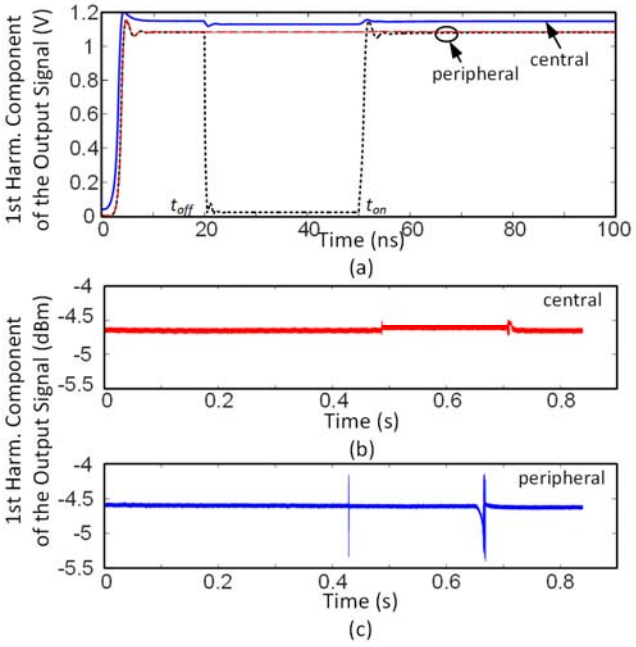


Fig. 17 Envelope-domain simulation of the coupled system, with an oscillator in an off state from $t_{off}$ = 20 ns to $t_{on}$ = 50 ns. Amplitude of the first harmonic component of the output signal of the different oscillators from the initial time $t$ = 0 ns value to 100 ns. (b) Measurement of the effect of switching *off* and *on* a peripheral oscillator on the central oscillator. (c) Measurement of the effect on one of the peripheral oscillators.

## III. Unilateral Injection

In this section, the central oscillator of the star topology is replaced by an independent source, which may consist of a phase-locked oscillator that cannot be influenced by the rest.

### A. *Steady-state analysis*

When replacing the central oscillator with an independent source, all the system oscillators are governed by the following steady-state equation:

$$Y_v \Delta V + Y_\omega \Delta\omega_s = A \frac{V_c}{V_o} e^{j(\phi_g - \alpha)} \tag{32}$$

where $V_c$ is the oscillation amplitude at the output of the central oscillator, acting as an independent source. Splitting the above system into real and imaginary parts one obtains:

$$Y_v^{\,r} \Delta V + Y_\omega^{\,r} \Delta\omega_s = A \frac{V_c}{V_o} \cos(\phi_g - \alpha) \tag{33a}$$

$$Y_v^{\,i} \Delta V + Y_\omega^{\,i} \Delta\omega_s = A \frac{V_c}{V_o} \sin(\phi_g - \alpha) \tag{33b}$$

For a given injection-source frequency $\omega_s$, the deviation $\Delta\omega_s$ is known and the system is easily solved for $\Delta V$ by

squaring and adding (a) and (b). Then the phase $\phi_g$ is directly calculated from (33). Following the indicated operations, $\Delta V$ is obtained from:

$$|Y_v|^2 \Delta V^2 + 2\left[(Y_v \cdot Y_\omega)\Delta\omega_s\right]\Delta V + \left(|Y_\omega|^2 \Delta\omega_s^2 - K^2\right) = 0 \quad (34)$$

where $K = AV_c / V_o$ and the operator $a \cdot b = a^r b^r + a^i b^i$ has been introduced. The amplitude deviation $\Delta V$ is given by:

$$\Delta V = \frac{-2|Y_\omega|\cos\alpha_{v,\omega}\Delta\omega_s \pm \sqrt{4|Y_\omega|^2 \Delta\omega_s^2(\cos^2\alpha_{v,\omega} - 1) + 4K^2}}{2|Y_v|} \quad (35)$$

The radicand must be positive for $\Delta V$ to be real, and there will be two values of $\Delta V$ for each distance $d$, respectively corresponding to the positive and negative signs before the root. Since $K$ is a proportional to $A$ and $V_c$, the magnitude of $\Delta V$ increases when reducing $d$ and increasing $V_c$. This effect can be seen in the analysis of Fig. 18. The source frequency is $f_s$ = 2.456 GHz and several values of $V_c$ have been considered, in the order of the output voltage of the oscillator elements. Results obtained with circuit-level HB simulation are superimposed with excellent agreement. The increase in $\Delta V$ when reducing $d$ (higher $K$) predicted by (35) can be noted. For very small $d$, the accuracy degrades due to the first-order approximation of the admittance functions. In Fig. 18, measurements have been superimposed, in the whole distance interval, for the lowest $V_c$ only, due to the space limitations in the experimental setup of Fig. 2.

Through inspection of (35), the two solutions coexisting for each $d$ merge into a single one when the radicand becomes zero:

$$4|Y_\omega|^2 \Delta\omega_s^2(\cos^2\alpha_{v,\omega} - 1) + 4K^2 = 0 \quad (36)$$

The above condition establishes the limit of existence of synchronized solutions. As shown in the next subsection, it corresponds to a turning-point bifurcation of the oscillator system, at which a real pole crosses through zero [35]-[37]. Taking (36) into account, as well as the definition of $K$, the maximum distance ($d_{max}$), up to which synchronized steady-state solutions can exist, is given by:

$$d_{\max} = \frac{V_c}{V_o}\frac{c\sqrt{G_{tot}}}{\omega_s R_r |Y_\omega||\Delta\omega_s|\sin\alpha_{v,\omega}} \quad (37)$$

The above expression for the maximum locking distance $d_{max}$ agrees with the one corresponding to the bilateral case, shown in (17), except for the additional factor $V_c / V_o$, corresponding to the ratio between the amplitude of the independent oscillator and the peripheral oscillators. The main difference between the bilateral and unilateral cases is not in this maximum locking distance, but in the stability properties of the locked solutions.

Note that the analysis above is immediately extended to a globally-coupled oscillator system with a symmetric topology, also having the injection-locked oscillator symmetrically located with respect to the rest. Following a derivation similar to the one in (18) to (20), the system should be formulated as:

$$Y_v^r \Delta V_p + Y_\omega^r \Delta\omega_s = \zeta(m, M-1)C_L + C_L e^{j\phi_c} V_c / V_o \quad (38)$$

The qualitative behaviour should be similar to the one described here, though each oscillation mode must be individually taken into account. As will be shown in the next sub-section, the unilateral system exhibits better stability properties, which is because the independent source is not affected by the coupling oscillator signals. However, in a general topology, having an independent source that is not symmetrically located with respect to the system oscillators, these oscillators will be subject to the influence of both the independent source and the coupling signals. Then, the overall behavior can be expected to be similar to the bilateral case considered in Section II.

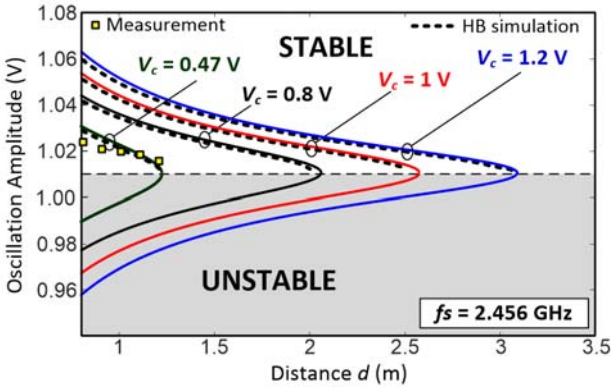


Fig. 18. Solution curves of the system when the central oscillator is replaced by an independent source. Four different values of $V_c$ have been considered, in the order of the system-oscillator amplitude. The source frequency is $f_s$ = 2.456 GHz. Results from circuit-level HB simulations are superimposed. Measurements are presented in the whole distance interval for the lowest $V_c$ only, due to the space limitations in the setup of Fig. 2.

## B. *Stability analysis*

For the stability analysis, a small perturbation is considered, following the same procedure as in Section II.B. This leads to the system:

$$\begin{bmatrix}\delta\dot{v}\\ \delta\dot{\phi}\end{bmatrix} = \begin{bmatrix}\frac{D_\omega^i}{V_o} & D_\omega^r\\ -\frac{D_\omega^r}{V_o} & D_\omega^i\end{bmatrix}^{-1}\begin{bmatrix}-Y_v^r & -D_\phi^r\\ -Y_v^i & -D_\phi^i\end{bmatrix}\begin{bmatrix}\delta v\\ \delta\phi\end{bmatrix} = [M_1]^{-1}[M_2]\begin{bmatrix}\delta v\\ \delta\phi\end{bmatrix} \quad (39)$$

where the matrixes $[M_1]$ and $[M_2]$ have been redefined for the new dimension-2 case and the following terms have been introduced:

$$C_L = Ae^{-j\alpha},\quad D_\omega = Y_\omega - \frac{\partial C_L}{\partial\omega}\frac{V_c}{V_o}e^{j\phi_g}$$
$$D_\phi = jC_L\frac{V_c}{V_o}e^{j\phi_g} \quad (40)$$

When varying the distance $d$ or any other parameter, a turning point will be obtained when the following condition is fulfilled:

$$\det\begin{bmatrix} -Y_v^{\,r} & -D_\phi^{\,r} \\ -Y_v^{\,i} & -D_\phi^{\,i} \end{bmatrix} = 0 \tag{41}$$

It is straightforward to obtain that (41) is equivalent to (37). In terms of the phase $\phi_g$, one can easily derive from (41) that the turning points fulfil:

$$\cos(\phi_g - \alpha - \alpha_v) = 0$$
$$\phi_g = \alpha + \alpha_v \pm \pi/2 \tag{42}$$

The analysis in (39) has been applied to the solution curve in Fig. 18, corresponding to $V_c$ = 1 V. The two poles predicted by (39) are real and have been represented versus $d$ in Fig. 19. The poles corresponding to the upper section of the solution curve are negative, so this section is stable. In contrast, the lower section exhibits a positive real pole, so this section is unstable. This pole becomes zero at the turning point where the two curve sections merge. The distance value $d_{max}$ at this turning point fulfils the condition (37).

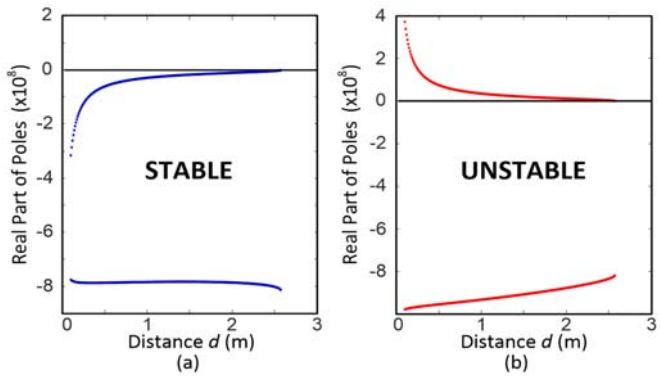


Fig. 19. Stability analysis of the curve corresponding to $V_c$ = 1 V and $f_s$ = 2.456 GHz. (a) Upper section of the curve (stable). (b) Lower section of the curve (unstable).

### C. Phase-noise analysis

The phase noise is calculated by considering the noise contribution of the individual-oscillator circuit $I_N(t)$, plus the phase noise due to the input source, given by $\psi(t)$. The total phase noise at any of the coupled oscillators is given by $\delta\phi_T = \delta\phi(t) + \psi(t)$. As stated in Section II.B, the time differentiator $s$, resulting from the frequency perturbation, gives rise to an instantaneous complex frequency that can be expressed as $\left(\dot{\psi} + \delta\dot{\phi}\right) - j\delta\dot{V}/V_o$. Thus, the noisy system is:

$$\begin{bmatrix} \dfrac{D_\omega^{\,i}}{V_o} & D_\omega^{\,r} \\ -\dfrac{D_\omega^{\,r}}{V_o} & D_\omega^{\,i} \end{bmatrix} \begin{bmatrix} \delta\dot{v} \\ \delta\dot{\phi} + \delta\dot{\psi} \end{bmatrix} = \begin{bmatrix} -Y_v^{\,r} & -D_\phi^{\,r} \\ -Y_v^{\,i} & -D_\phi^{\,i} \end{bmatrix} \begin{bmatrix} \delta v \\ \delta\phi \end{bmatrix} + \begin{bmatrix} I_N^r \\ I_N^i \end{bmatrix} \tag{43}$$

Calculating the Fourier transform and solving for $\Delta\phi_T(\Omega)$, one obtains:

$$\Delta\phi_T(\Omega) = \frac{Y_v \times I_N + j\Omega\dfrac{D_\omega \cdot I_N}{V_o} - \left(Y_v \times D_\phi + j\Omega\dfrac{D_\omega \cdot D_\phi}{V_o}\right)\psi(\Omega)}{-\Omega^2\dfrac{|D_\omega|^2}{V_o} + \left(Y_v \times D_\omega - \dfrac{D_\omega \cdot D_\phi}{V_o}\right)j\Omega - Y_v \times D_\phi} \tag{44}$$

where the following general operators have been used: $a \times b = a^r b^i - a^i b^r$ and $a \cdot b = a^r b^r + a^i b^i$. The phase noise spectral density is obtained multiplying (44) by $\Delta\phi_T^{\,*}(\Omega)$, taking into account that the oscillator noise sources and the phase noise from the synchronizing source are uncorrelated. Neglecting higher order terms in the perturbation frequency Ω one obtains the expression:

$$\left|\Delta\phi_T(\Omega)\right|^2 = \frac{2|Y_V|^2\dfrac{|I_N|^2}{V_o^2} + |Y_V \times D_\phi|^2\,|\psi(\Omega)|^2}{|Y_v \times D_\phi|^2 + \left[\left(Y_v \times D_\omega - \dfrac{D_\omega \cdot D_\phi}{V_o}\right)^2 + 2\,Y_v \times D_\phi\,\dfrac{|D_\omega|^2}{V_o}\right]\Omega^2} \tag{45}$$

At small offset frequency Ω, and assuming a larger noise level in the input-source phase $\psi(\Omega)$ than in the circuit equivalent noise source $I_N$, the oscillator spectrum will initially follow $\psi(\Omega)$. Then, it will follow the circuit own noise source and, finally, at larger offset frequencies, it will decay as -20 dB/dec. Expression (45) predicts two distinct corner frequencies in the phase noise spectrum. It follows the phase noise of the independent source up to (approximately) the first corner $\Omega_1$. This is obtained when the two terms in the numerator become equal, so it fulfils the condition:

$$|\psi(\Omega_1)|^2 = \frac{2|Y_V|^2}{|Y_V \times D_\phi|^2}\frac{|I_N|^2}{V_o^2} = \frac{2|I_N|^2}{V_c^2 A^2 \sin^2(\alpha_{D\phi} - \alpha_v)} \tag{46}$$

where $\alpha_{D\phi}$ is the angle of $D_\phi$. This corner increases with the coupling magnitude $A$ and $V_c$ since, for a given input phase-noise spectrum $|\psi(\Omega)|^2$ the offset frequency has to reach a higher value in order to fulfil (46). Note that $A$ decreases with $d$, so a lower corner frequency $\Omega_1$ may be expected when increasing $d$. However, there is also a sinusoidal dependence through the angle $\alpha_{D\phi}$. The second corner frequency $\Omega_2$ is obtained when the two terms in the denominator become equal. From inspection of (45), this is inversely proportional to $|D_\omega|$, defined in (40).

The above analysis method has been applied to the coupled-oscillator system obtained by replacing the central oscillator with an independent source. The input frequency is $f_s$ = 2.452 GHz and the distance is $d$ = 0.85 m. In Fig. 20, the resulting phase-noise spectral density is compared with the one obtained in the bilateral case, with similar results. Note that the same

injection source with the same phase noise $\psi(t)$ is used in the two cases. In the intermediate offset-frequency interval, the phase noise of the peripheral oscillator is slightly higher than in the central oscillator. There is an excellent agreement with the experimental results obtained with the equipment R&S FSWP.

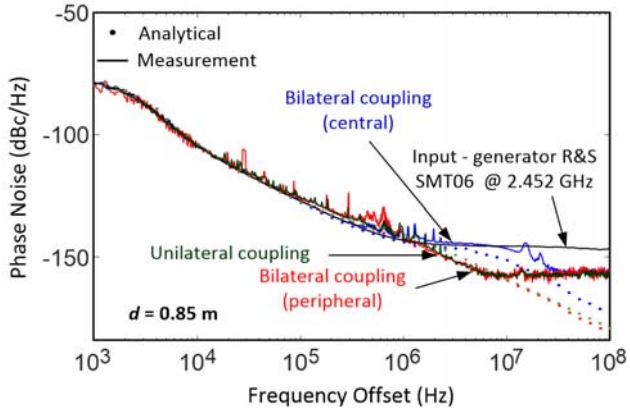


Fig. 20. Comparison of the phase-noise spectrum under unilateral and bilateral coupling. The distance ($d$ = 0.85 m) to the central node, the injection amplitude and the input phase noise $\psi(t)$ are the same in the two cases.

## IV. Conclusion

An investigation of the steady-state solutions, stability and phase noise of wireless-coupled oscillators under the effect of an injection-locking signal has been presented. The analytical formulation is based on oscillator models extracted from harmonic balance and uses a realistic description of the propagation effects. Two cases have been distinguished: bilateral synchronization, in which an injection source is connected to one oscillator element, coupled to the rest, and unilateral synchronization, in which an injection source replaces one of the system oscillators. The coupled system has been particularized to the case of a star topology. In both the bilateral and the unilateral cases, synchronized solutions only exist only up to a maximum distance between the central node and the rest. The pattern of the steady-state solutions in terms of the oscillation frequency and amplitude is oscillatory in the case of bilateral synchronization and monotonous in the case of unilateral synchronization. A closed form expression has been derived for the maximum locking distance in the two cases. Unlike the situation in free-running coupled systems, where stable and unstable distances intervals alternate, from certain amplitude of the injection source, the system stabilizes up to a maximum distance, without an alternation of stable/unstable intervals. The phase noise considerably decreases with respect to the one obtained in free-running operation. The bilateral case is more general since, when having an independent source that is not symmetrically located with respect to the system oscillators, these oscillators will be subject to the influence of both the independent source and the coupling signals.

## References


[1] O. Simeone, U. Spagnolini, Y. Bar-Ness, and S. H. Strogatz, "Distributed synchronization in wireless networks," *IEEE Signal Process. Mag*., vol. 25, no. 5, pp. 81-97, Sep. 2008.

[2] D. J. Jörg et al., "Synchronization of mutually coupled digital PLLs in massive MIMO systems," *IEEE Int. Conf. Commun.*, London, UK, 2015, pp. 1716-1721.

[3] O. Simenone and U. Spagnolini, "Distributed synchronization for wireless sensor networks with coupled discrete-time oscillators, *Eurasip J. Wireless Commun. Networking*, #57054, 2007.

[4] S. Barbarossa and G. Scutari, "Decentralized maximum likelihood estimation for sensor networks composed of nonlinearly coupled dynamical systems," *IEEE Trans. Signal Process.*, vol. 55, no. 7, pp. 3456-3470, Jul. 2007.

[5] A. Mauroy, P. Sacré, and R. Sepulchre, "Kick synchronization versus diffusive synchronization," 51st *IEEE Conf. Decision and Control* (CDC), Maui, HI, 2012, pp. 7171-7183.

[6] K. Matsuzaka, K. Nakada, and T. Morie, "Analog CMOS circuit implementation of a system of pulse-coupled oscillators for spike-based computation," *IEEE Int. Symp. Circuits Syst.* (*ISCAS*), Rio de Janeiro, 2011, pp. 2849-2852.

[7] E. Mallada, R. A. Freeman, and A. K. Tang, "Distributed Synchronization of Heterogeneous Oscillators on Networks With Arbitrary Topology," *IEEE Trans. Control Netw. Syst.*, vol. 3, no. 1, pp. 12-23, Mar. 2016.

[8] Y. Wang, F. Nunez and F. J. Doyle, "Energy-Efficient Pulse-Coupled Synchronization Strategy Design for Wireless Sensor Networks Through Reduced Idle Listening," *IEEE Trans. Signal Proces.*, vol. 60, no. 10, pp. 5293-5306, Oct. 2012.

[9] O. Simeone and G. Scutari, "Pulse-coupled distributed PLLs in heterogeneous wireless networks," *2007 Conference Record of the Forty-First Asilomar Conference on Signals, Systems and Computers*, Pacific Grove, CA, 2007, pp. 1770-1775.

[10] C. H. Rentel and T. Kunz, "A Mutual Network Synchronization Method for Wireless Ad Hoc and Sensor Networks," *IEEE Trans. Mobile Comput.*, vol. 7, no. 5, pp. 633-646, May 2008.

[11] E. Mallada, X. Meng, M. Hack, L. Zhang and A. Tang, "Skewless Network Clock Synchronization Without Discontinuity: Convergence and Performance," in *IEEE/ACM Trans. Netw.*, vol. 23, no. 5, pp. 1619-1633, Oct. 2015.

[12] A. Gushchin, E. Mallada and A. Tang, "Phase-Coupled Oscillators with Plastic Coupling: Synchronization and Stability," *IEEE Trans. Netw. Sci. Eng.*, vol. 3, no. 4, pp. 240-256, Oct.-Dec. 1 2016.

[13] A. Díaz-Guilera, A. Arenas, *Phase patterns of coupled oscillators with application to wireless communication*, P. Lio, *et al.* (Eds.), BIOWIRE 2007, LNCS, vol. 5151, Springer-Verlag, Berlin (2008), pp. 172-179.

[14] M. Pontón and A. Suárez, "Stability analysis of wireless coupled–oscillator circuits," *IEEE MTT-S Int. Microwave Symp.,* Honolulu, Hawaii, Jun. 2017.

[15] M. Pontón and A. Suárez, "Oscillation Modes in Symmetrical Wireless-Locked Systems," *IEEE Trans. Microw.Theory Techn*., vol. 66, no. 5, pp. 2495-2510, May 2018.

[16] R. A. York, "Nonlinear analysis of phase relationships in quasi-optical oscillator arrays," *IEEE Trans. Microw. Theory Techn.*, vol. 41, pp. 1799–1809, Oct. 1993.

[17] R. A. York and T. Itoh, "Injection- and phase-locking techniques for beam control," *IEEE Trans. Microw. Theory Techn.*, vol. 46, pp. 1920–1929, 1998.

[18] T. Heath, R. R. Kerr, and G. D. Hopkins, Two-dimensional, nonlinear oscillator array antenna, *IEEE Aerosp. Conf.*, pp. 1104–1115, 2005.

[19] T. Heath, R. R. Kerr, and G. D. Hopkins, "Nonlinear oscillator array antenna development at GTRI," *IEEE Aerosp. Conf.*, p. 19, 2006.

[20] A. Suárez, F. Ramírez and S. Sancho, "Stability and Noise Analysis of Coupled-Oscillator Systems," *IEEE Trans. Microw. Theory Techn.*, vol. 59, no. 4, pp. 1032-1046, Apr. 2011.

[21] A. Suárez, F. Ramírez, S. Sancho, J.M. Collantes, "Global stability analysis of coupled-oscillator systems," *IEEE Trans. Microw. Theory Techn*., vol. 63, no. 1, pp. 165 - 180, Jan. 2015.

[22] A. Suárez, S. Sancho, F. Ramírez, "General Formulation for the Analysis of Injection-Locked Coupled-Oscillator Systems," *IEEE Trans. Microw. Theory Techn*., vol. 61, no. 12, pp. 4730-4744, Dec., 2013.

[23] Y. M. Tousi V. Pourahmad E. Afshari "Frequency tuning of terahertz sources using delay-coupled oscillators" *Phys. Rev. Lett.* vol. 108 pp. 234101.1-234101.5 Jun. 2012.

[24] M. Adnan and E. Afshari, "A 105-GHz VCO with 9.5% Tuning Range and 2.8-mW Peak Output Power in a 65-nm Bulk CMOS Process," *IEEE Trans. Microw. Theory Techn*., vol. 62, no. 4, pp. 753-762, April 2014.

[25] A. Tyrrell and G. Auer, "Imposing a Reference Timing onto Firefly Synchronization in Wireless Networks," *2007 IEEE 65th Vehicular Technology Conference - VTC2007-Spring*, Dublin, 2007, pp. 222-226.
[26] Alexander Tyrrell, Gunther Auer, "Biologically Inspired Intercellular Slot Synchronization," *EURASIP Journal on Wireless Communications and Networking*, Dec. 2009.
[27] Hai-Lin Zou, Zi-Chen Deng, Wei-Peng Hu, Ying-Cheng Lai, "Partially unstable attractors in networks of forced integrate-and-fire oscillators," *Nonlinear Dynamics*, April 2017.
[28] M. Pontón and A. Suárez, "Wireless Injection Locking of Oscillator Circuits," *IEEE Trans. Microw. Theory Techn*., vol. 64, no. 12, pp. 4646-4659, Dec. 2016.
[29] F. Ramírez, E. de Cos and A. Suárez, "Nonlinear analysis tools for the optimized design of harmonic-injection frequency dividers", *IEEE Trans. Microw. Theory Techn.*, vol. 51, no. 6, pp. 1752-1762, Jun. 2003.
[30] K. Kurokawa, "Some basic characteristics of broadband negative resistance oscillators", *Bell Syst. Tech. J*., vol. 48, pp. 1937–1955, July–Aug. 1969.
[31] A. Suarez and R. Melville, "Simulation-assisted design and analysis of varactor-based frequency multipliers and dividers," *IEEE Trans. Microw. Theory Techn*., vol. 54, no. 3, pp. 1166-1179, March 2006.
[32] S. ver Hoeye, L. Zurdo and A. Suarez, "New nonlinear design tools for self-oscillating mixers," *IEEE Microwave and Wireless Components Letters*, vol. 11, no. 8, pp. 337-339, Aug. 2001.
[33] A. Suárez, *Analysis and Design of Autonomous Microwave Circuits*. Hoboken, NJ: Wiley IEEE Pres, 2009.
[34] K. Kurokawa, "An Analysis of Rucker's Multidevice Symmetrical Oscillator," *IEEE Trans. Microw. Theory Techn.,* vol. 18, pp. 967, May. 1970.
[35] J. Guckenheimer and P. Holmes, *Nonlinear Oscillations, Dynamical Systems and Bifurcations of Vector Fields*. New York: Springer-Verlag, 1990.
[36] A. Suarez, J. Morales and R. Quere, "Synchronization analysis of autonomous microwave circuits using new global-stability analysis tools," *IEEE Trans. Microw. Theory Techn.*, vol. 46, no. 5, pp. 494-504, May 1998.
[37] V. Rizzoli and A. Neri, "State of the art and present trends in nonlinear microwave CAD techniques," *IEEE Trans. Microw. Theory Techn.*, vol. 36, no. 2, pp. 343-365, Feb 1988.
[38] R. Quere, E. Ngoya, M. Camiade, A. Suarez, M. Hessane, and J. Obregon, "Large signal design of broadband monolithic microwave frequency dividers and phase-locked oscillators," *IEEE Trans. Microw. Theory Techn.*, vol. 41, no. 11, pp. 1928-1938, Nov. 1993.
[39] F. Ramírez, M. Pontón, S. Sancho, and A. Suárez, "Phase−Noise Analysis of Injection−Locked Oscillators and Analog Frequency Dividers", *IEEE Trans. Microw. Theory Techn*., vol. 56, no.2, pp. 393−407, 2008.
[40] K. Kurokawa, "Noise in synchronized oscillators," *IEEE Trans. Microw. Theory Techn*., vol. MTT-16, no. 4, pp. 234–240, Apr. 1968.
[41] S. Sancho, A. Suárez and F. Ramírez, "General phase-noise analysis from the variance of the phase deviation," 2012 *IEEE/MTT-S Int. Microw. Sympo. Digest, Montreal*, QC, 2012, pp. 1-3.
[42] B. Razavi, "A study of injection locking and pulling in oscillators," *IEEE Journal of Solid-State Circuits*, vol. 39, no. 9, pp. 1415-1424, Sept. 2004.
[43] S. Sancho, M. Ponton, A. Suarez and F. Ramirez, "Analysis of Injection Pulling in Phase-Locked Loops with a New Modeling Technique," *IEEE Trans. Microw. Theory Techn*., vol. 61, no. 3, pp. 1200-1214, March 2013.
[44] J. Dominguez, A. Suarez and S. Sancho, "Semi-analytical formulation for the analysis and reduction of injection-pulling in front-end oscillators," 2009 *IEEE MTT-S Int. Microw. Symp. Digest*, Boston, MA, pp. 1589-1592.
[45] E. Ngoya and R. Larcheveque, "Envelope transient analysis: A new method for the transient and steady state analysis of microwave communication circuits and systems," *IEEE MTT-S Int. Microw. Symp. Dig.*, San Francisco, CA, USA, Jun. 1996, vol. 3, pp. 1365–1368.
[46] J. C. Pedro and N. B. Carvalho, "Simulation of RF circuits driven by modulated signals without bandwidth constraints," *IEEE MTT-S Int. Microw. Symp. Dig.*, Seattle, WA, USA, 2002, pp. 2173–2176.
[47] E. de Cos, A. Suárez, and S. Sancho, "Envelope transient analysis of self-oscillating mixers," *IEEE Trans. Microw. Theory Techn.*, vol. 52, no. 4, pp. 1090–1100, Apr. 2004.

**Mabel Pontón** (S'08–M'11) was born in Santander, Spain. She received the bachelor's degree in Telecommunication Engineering, master's degree in Information Technologies and Wireless Communications Systems, and Ph.D. degree from the University of Cantabria, Santander, in 2004, 2008, and 2010, respectively. In 2006, she joined the Communications Engineering Department, University of Cantabria.

From 2011 to 2013, she was with the Group of Electronic Design and Applications, Georgia Institute of Technology, Atlanta, GA, USA, as a Post-Doctoral Research Fellow.

Her current research interests include the nonlinear analysis and simulation of radiofrequency and microwave circuits, with an emphasis on phase-noise, stability, and bifurcation analysis of complex oscillator topologies.

**Amparo Herrera** was born in Asturias (Spain) in 1963. She received the degree in Electronic Physics from the University of Cantabria (Spain) in June 1987, and the Ph.D degree from the same University in June 1995. In 1987 she joined the CIDA (Centro de Investigación y Desarrollo de la Armada) the Research and Development Spanish Army Centre, working on developing a RF&Microwave laboratory up to 1990 when she joined the Electronics Department of the University of Cantabria, working on MMIC design. From 1992 to 1995, she collaborated with the Laboratory Philips Microwave Limeil (actually OMMIC), as result of this collaboration she presents her thesis receiving the Ph.D. degree in Electronics from the University of Cantabria in June 1995 in this work she had designed a high efficiency power amplifier for DECT and DCS applications a work for the Philips Microwave Limeill foundry (now called OMMIC). From 1995 she has been an associate professor at the University of Cantabria, and a member of its Communications Engineering Department. Her areas of interest include the MMIC and Hybrid design of microwave circuits and, specially, the power and low noise amplifier design and characterization. She has taken part as Main researcher in a big number of Spanish and European projects both of the III, IV, V and VI Frameworks and Spanish National R&D Plan. Also she has participated in a number of industrial projects with European and Spanish industries. Currently she is working in the design and development of MMIC devices on Si-Ge, GaN PHEMT technologies.

**Almudena Suárez** (M'96–SM'01–F'12) was born in Santander, Spain. She received the Electronic Physics and Ph.D. degrees from the University of Cantabria, Santander, Spain, in 1987 and 1992, respectively, and the Ph.D. degree in Electronics from the University of Limoges, Limoges, France, in 1993.

She is currently a Full Professor with the Communications Engineering Department, University of Cantabria. She co-authored *Stability Analysis of Nonlinear Microwave Circuits* (Artech House, 2003) and authored *Analysis and Design of Autonomous Microwave Circuits* (IEEE-Wiley, 2009).

Prof. Suárez is a member of the Technical Committees of the IEEE Microwave Theory and Techniques Society (IEEE MTT-S) International Microwave Symposium (IMS) and the European Microwave Conference. She was an IEEE Distinguished Microwave Lecturer from 2006 to 2008. She is a member of the Board of Directors of the European Microwave Association. She was the Coordinator of the Communications and Electronic Technology Area for the Spanish National Evaluation and Foresight Agency between 2009 and 2013. In 2014 and 2015 she was the co-chair of IEEE Topical Conference on RF Power Amplifiers (PAWR). Prof. Suárez is the Editor-in-Chief of the International Journal of Microwave and Wireless Technologies from Cambridge University Press journals and an Associate Editor for IEEE Microwave Magazine.